N81- 18035

NASA Contractor Report 165658

Failure Detection and Isolation Analysis of a Redundant Strapdown Inertial Measurement Unit

P. Motyka, M. Landey, R.McKern

The Charles Stark Draper Laboratory, Inc.
Cambridge, Massachusetts 02139

NASA

National Aeronautics and
Space Administration

Langley Research Center
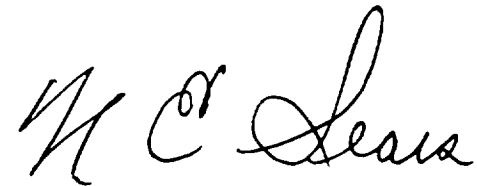Hampton, Virginia 23665

R-1414

FAILURE DETECTION AND ISOLATION
ANALYSIS OF A REDUNDANT
STRAPDOWN INERTIAL MEASUREMENT UNIT

by

P. Motyka
M. Landey
R. McKern

February 1981

Approved: _____

N.E. Sears

The Charles Stark Draper Laboratory, Inc.
Cambridge, Massachusetts 02139

TABLE OF CONTENTS

LIST OF ACRONYMS

BITE	built-in test equipment
CTOL	conventional takeoff or landing
CSDL	The Charles Stark Draper Laboratory, Inc.
EVT	Edge Vector Test
FDI	failure detection and isolation
GLT	Generalized Likelihood Test
IMU	inertial measurement unit
NASA	National Aeronautics and Space Administration
SDOF	single degree of freedom
TDOF	two degree of freedom

LIST OF SYMBOLS

AC	accelerometer input-axis acceleration including misalignment effects (g)
ACI	trapezoidal integrated value of AC (m/s)
ACIL	lagged value of ACI (m/s)
ACP	accelerometer pendulous-axis acceleration (g)
ACPI	trapezoidal integrated value of ACP (m/s)
ACPIL	lagged value of ACPI (m/s)
ACT	acceleration signal (pulses)
AGY	acceleration along gyro input or spin axes (g)
AGYI	trapezoidal integrated value of AGY (m/s)
AQF	fractional value of ACT (pulses)
AQI	integer value of ACT (pulses)
Ai, Bi	two input axes of instruments, $i = 1,2,3,4$
$\bar{a}$, $\bar{b}$	constants: $\sqrt{3} + 1$ and $\sqrt{3} - 1$, respectively
b	magnitude of bias failure (rad)
DF_D	failure decision function (rad^2 or $(m/s)^2$)
DF_{I_j}	failure isolation function for the jth sensor (rad^2 or $(m/s)^2$)
DT	computation time interval (s)
DTR	conversion factor from degrees to radians ($\pi/180°$)
E_{ij}	constant: $2\sqrt{3}\ \zeta_{ij}$
$\hat{e}_{ij}$	edge vectors relating instruments, $i,j = 1,2,3,4$

f	magnitude of failure (rad or m/s)
G, F	logical variables in edge vector algorithm used to detect and isolate failures
GCT	gyro signal (pulses)
GCTL	lagged value of GCT (pulses)
GQF	fractional value of GCTL
GQI	integer value of GCTL (pulses)
GY	gyro input-axis angular rate including misalignment (°/s)
GYI	trapezoidal integrated value of GY (rad)
Gϕ	gravitational constant (9.8062 $m/s^2/g$ (32.1725 $ft/s^2/g$))
$\hat{H}$	transformation matrix
h	altitude (m)
M	Mach number
$\hat{m}$	n vector of measurements (rad or m/s)
$\tilde{m}$	sensor errors (rad or m/s)
n	number of sensors
n_x, n_y, n_z	longitudinal, lateral, and normal body-axes linear inertial accelerations (g)
P	probability of event occurring
p, q, r	body axes roll, pitch, yaw rates (°/s)
R	edge vector algorithm parity-equation residuals
SF	scale factor (pulses/$\overline{sec}$ or pulses/m/s)
S_i	spin axis of instrument i
T	failure-detection threshold
TDF	two-degree-of-freedom gyro errors (rad)
T_0	constant portion of threshold (rad^2 or $(m/s)^2$)
T_{90}	time for filter to reach 90 percent of its final value (s)

$\hat{V}$	$(n - 3) \times n$ matrix of parity equations
$\hat{V}_j$	jth column of V
x, y, z	axes system components
x_o	offset of IMU from vehicle centerline (m)
x_s	separation of IMU1, IMU2 from IMU centerline (m)
α_{IP}	accelerometer input-pendulous-axes cross-coupling error ($\mu g/g^2$)
β_{II}	accelerometer input-axes-squared error ($\mu g/g^2$)
δ_g	two-degree-of-freedom-gyro acceleration error coefficient ($°/s/g$ or $°/s/g^2$)
$\delta_{g_{\ell m}}$	upper bound for $\delta_{g_{j1}} + \delta_{g_{j2}} + \delta_{g_{j3}}$ ($°/s/g$)
$\delta_{g_{nm}}$	upper bound for $\delta_{g_{j4}} + \delta_{g_{j6}} + \delta_{g_{j7}} + \delta_{g_{j8}} + \delta_{g_{j9}}$ ($°/s/g^2$)
δ_n	two-degree-of-freedom-gyro angular rate error coefficient ($°/s/(rad/s)^2$)
δ_{n_m}	upper bound for $\delta_{n_{j8}} + \delta_{n_{j9}}$ ($°/s/(rad/s)^2$)
ϵ	scale-factor error (ppm)
ζ	uncertainties in instrument measurements
$\hat{\eta}$	n vector of measurement noise which is Gaussian with zero mean and covariance matrix R
λ	bias error ($°/s$ or μg)
μ	misalignment error (rad)
$\hat{\rho}$	n-3 vector of GLT parity-equation residuals (rad or m/s)
σ	standard deviation
τ	filter time constant (s)
$\hat{\omega}$	three-dimensional vector of body-axes inertial linear accelerations (g) or angular rates ($°/s$)
ω_{ij}^B	body axes component of sensed angular rate of ith instrument along jth axes (rad)

Subscripts

A	accelerometer-axes system
a	accelerometer
B	body-axes system
F	presence of failed sensor
FA	false alarm
f	filtered
G	gyro-axes system
g	gyro
h	hard-failure channel
II	input-axes squared
IP	input pendulous axes
i, j, k, ℓ	element number, row, and/or column indicator of matrices or vectors
M	IMU-axes system
m	positive maximum or upper bound
N	absence of failed sensor
n	iteration number
P	pendulous-axes system
S	spin-axes system
s	soft-failure channel
O	initial condition

Superscripts

A	accelerometer-axes system
B	body-axes system
G	gyro-axes system
M	IMU-axes system
P	pendulous-axes system
S	spin-axes system
T	transpose
$(\tilde{})$	error
$(\hat{})$	vector or matrix

SECTION 1

INTRODUCTION

One way to lower the cost of aircraft is to improve the integration of avionics functions. Currently, there is considerable interest in replacing the multiple flight-control sensors of a typical modern commercial aircraft with a skewed array of strapdown inertial navigation sensors, using redundant computers to perform multiple functions such as flight control, air-data processing, and strapdown navigation. Net cost has been shown to be less than for current nonintegrated systems. This integrated avionics approach depends upon redundancy to achieve the reliability needed in flight-control loops. In order to achieve various performance and economic improvements, the next generation of aircraft will be designed to depend upon the flight-control avionics for flight stability. Because flight-control-system reliability and safety depend upon integrated avionics reliability, thorough analysis of skewed-sensor-system reliability is therefore essential.

The objective of this study was to define and develop techniques which will be the basis for failure-detection and isolation (FDI) algorithms for a NASA-owned dual-fail/operational redundant strapdown inertial navigation system. These techniques will provide the government with the capability for testing and evaluating dual-fail/operational concepts. The FDI techniques chosen include provisions for hard- and soft-failure detection in the context of flight control and navigation. The algorithms are of minimum complexity, suitable for flight testing. Analyses were done to determine error-detection and switching levels for the inertial navigation system, which is intended to be of 5- to 10-kilometer- (3- to 5-nautical-mile-) per-hour quality for a conventional takeoff

1

or landing (CTOL) operating environment. Analyses of false alarms are also included for the FDI techniques developed, as are the analyses of filters to be used in conjunction with FDI processing.

Two specific FDI algorithms were compared in this study: the Generalized Likelihood Test (GLT) and the Edge Vector Test (EVT). They are compared with regard to:

(1)   The systems of parity equations required for FDI.

(2)   The ability to correctly detect and isolate failures.

(3)   The possible thresholds and failure-detection levels.

(4)   The need for dynamic thresholds.

(5)   The development and evaluation of techniques for generating these thresholds.

(6)   The software requirements.

A deterministic digital computer simulation was used to compare and evaluate the algorithms and FDI systems. The evaluation trajectory used incorporates features typical of a transport aircraft flight profile. Time histories of variables pertinent to the evaluation of the algorithms were taken.

The report has the following general outline. A description of the redundant sensor configuration is presented first. This is followed by a general description of material used in the evaluation of the algorithms, such as the simulation, instrument models, evaluation trajectory, philosophy of FDI, and approach to generating the thresholds. An analysis of the two algorithms—EVT and GLT—follows, and a comparison of the advantages and disadvantages of the algorithms is made.

The measurements reported in SI units were originally made in English units and translated; the original units are given throughout the report in parentheses.

SECTION 2

THE SENSOR CONFIGURATION

The inertial measurement unit (IMU)[1]* is a redundant strap-
down package employing four two-degree-of-freedom (TDOF) gyros
(accelerometers) in a semi-octahedral geometry. The instruments are
positioned such that the spin (pendulous) axes are normal to the four
faces of the semi-octahedron and point out. The two measurement axes
of the gyro lie in the plane of the face and are symmetric about the
face centerline. The IMU consists of two separate packages (faces 1
and 2, faces 3 and 4) which may be spatially separated along a track
in the y_B direction. Thus, it may be treated as two tetradic IMUs.
It has been demonstrated[12] that FDI will be more effective if the
two tetradic IMUs are treated as a single IMU, and that approach is
taken here. (The effects of a large separation have not been addressed
in this work.)

Two axes systems are defined: the body frame (B) and the IMU
frame (M), as shown in Figures 1 and 2. The body frame is the conven-
tional x_B (roll), y_B (pitch), z_B (yaw) axes system. The IMU frame is
a triad, with x_M along the track separating the two tetrads and positive
toward the right wing and y_M along the junction of IMUs 1 and 2, par-
allel to the vehicle centerline, and positive forward; z_M completes the
triad.

_____

*Superscript numerals refer to similarly numbered items in the List of
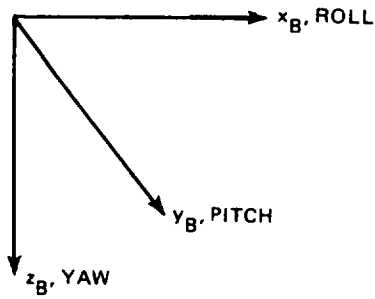 References.

3

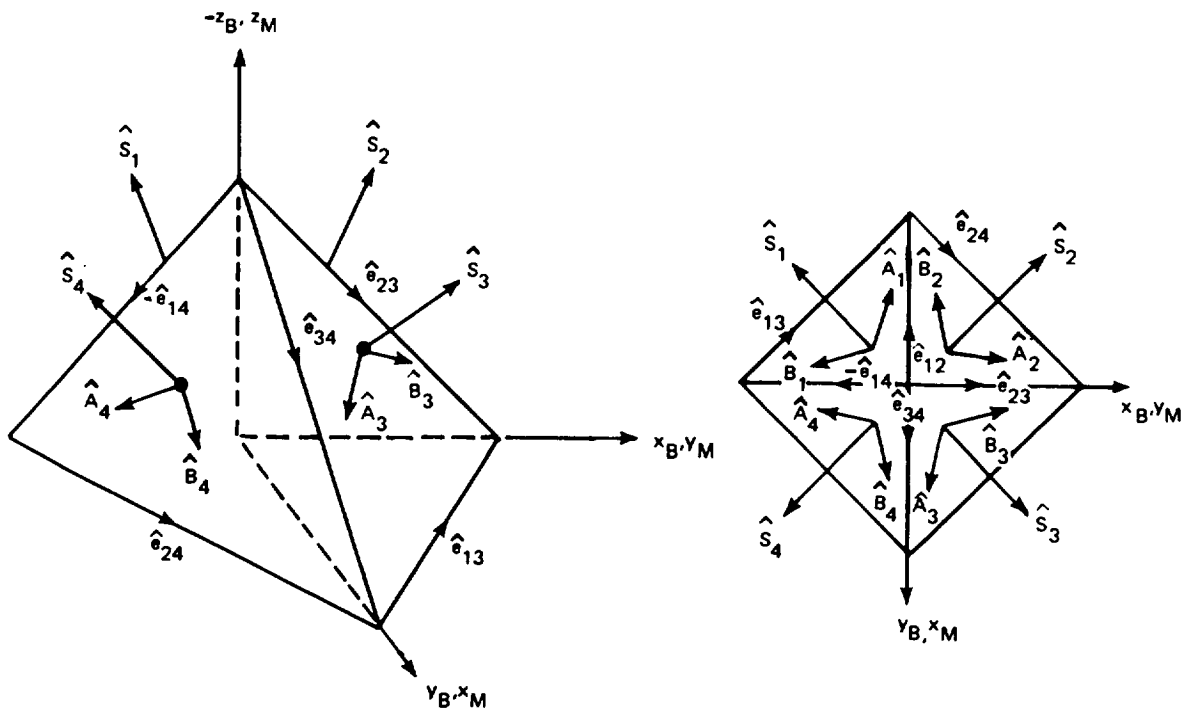Figure 1. Body-axes system definition.

Figure 2. IMU instrument geometry.

4

Neglecting any mounting misalignments of the IMU, the rotation from the body frame to the IMU frame may be represented by the matrix.

$$\hat{H}_B^M = \begin{bmatrix} 0 & 1 & 0 \\ 1 & 0 & 0 \\ 0 & 0 & -1 \end{bmatrix}$$

For an ideal system, with all misalignments identically zero, the spin axes and pendulous axes are coincident with the outer normals to the octahedron faces, as indicated in Figure 2.

The matrix $\hat{H}_M^S$ defines the nominal transformation from the IMU frame (x_M, y_M, z_M) to the nonorthogonal spin axes $(S_1, \ldots, S_4)$

$$\hat{H}_M^S = \frac{1}{\sqrt{3}} \begin{bmatrix} -1 & -1 & 1 \\ -1 & 1 & 1 \\ \hline 1 & 1 & 1 \\ 1 & -1 & 1 \end{bmatrix}$$

The transformation from the IMU frame to the pendulous axes, $\hat{H}_M^P$, is defined by

$$\hat{H}_M^P \equiv \hat{H}_M^S$$

Postmultiplying by $\hat{H}_B^M$ yields

$$\hat{H}_B^S = \frac{1}{\sqrt{3}} \begin{bmatrix} -1 & -1 & -1 \\ 1 & -1 & -1 \\ \hline 1 & 1 & -1 \\ -1 & 1 & -1 \end{bmatrix} = \begin{bmatrix} \hat{S}_1^T \\ \hat{S}_2^T \\ \hline \hat{S}_3^T \\ \hat{S}_4^T \end{bmatrix}$$

and similarly for $\hat{H}_B^P$. Considering the octahedron as two IMUs, the spin (pendulous) axes of IMUs 1 and 2 are represented by the top and bottom halves of these matrices, respectively. Figure 3 also indicates this separation.
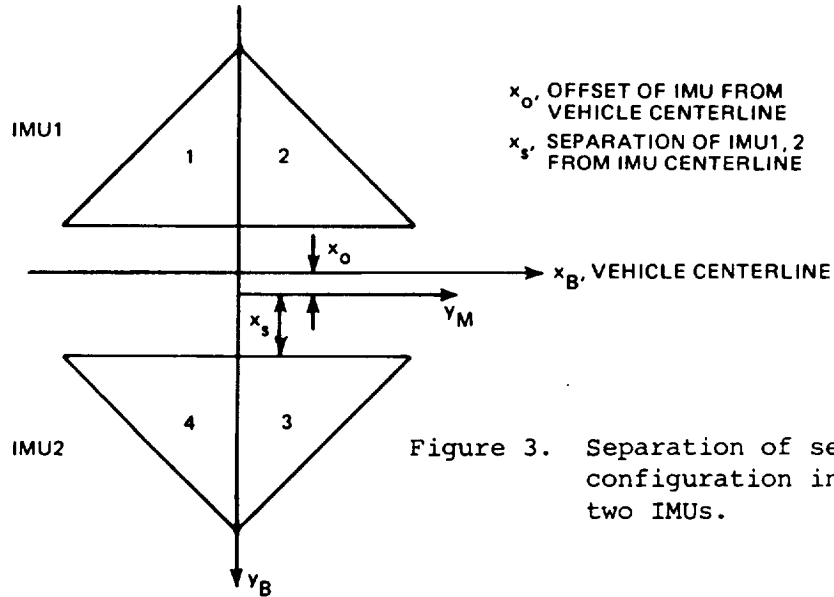

Figure 3. Separation of sensor configuration into two IMUs.

The ideal transformation from the IMU frame (x_M, y_M, z_M) to the nonorthogonal sensor axes $(\hat{A}_1, \hat{B}_1, \ldots, \hat{B}_4)$ may also be written as

$$
\hat{H}_M^G = \frac{1}{2\sqrt{3}}
\begin{bmatrix}
-\sqrt{3} - 1 & \sqrt{3} - 1 & -2 \\
\sqrt{3} - 1 & -\sqrt{3} - 1 & -2 \\
\sqrt{3} - 1 & \sqrt{3} + 1 & -2 \\
-\sqrt{3} - 1 & -\sqrt{3} + 1 & -2 \\
\hline
\sqrt{3} + 1 & -\sqrt{3} + 1 & -2 \\
-\sqrt{3} + 1 & \sqrt{3} + 1 & -2 \\
-\sqrt{3} + 1 & -\sqrt{3} - 1 & -2 \\
\sqrt{3} + 1 & \sqrt{3} - 1 & -2
\end{bmatrix}
=
\begin{bmatrix}
\hat{A}_1 \\
\hat{B}_1 \\
\hat{A}_2 \\
\hat{B}_2 \\
\hline
\hat{A}_3 \\
\hat{B}_3 \\
\hat{A}_4 \\
\hat{B}_4
\end{bmatrix}
$$

with the accelerometer measurement axes given by

$$\hat{H}^A_M \equiv \hat{H}^G_M$$

Again, IMUs 1 and 2 are represented by the top and bottom halves of $\hat{H}^G_M$, respectively. The transformation from the body frame to the sensor axes is given by

$$\hat{H}^A_B = \hat{H}^G_B = \frac{1}{2\sqrt{3}} \left[\begin{array}{ccc} \sqrt{3} - 1 & -\sqrt{3} - 1 & 2 \\ -\sqrt{3} - 1 & \sqrt{3} - 1 & 2 \\ \sqrt{3} + 1 & \sqrt{3} - 1 & 2 \\ -\sqrt{3} + 1 & -\sqrt{3} - 1 & 2 \\ \hline -\sqrt{3} + 1 & \sqrt{3} + 1 & 2 \\ \sqrt{3} + 1 & -\sqrt{3} + 1 & 2 \\ -\sqrt{3} - 1 & -\sqrt{3} + 1 & 2 \\ \sqrt{3} - 1 & \sqrt{3} + 1 & 2 \end{array} \right]$$

SECTION 3

SIMULATION FEATURES AND INPUTS

The results of this study were obtained from a deterministic digital simulation. A block diagram of this simulation is presented in Figure 4 (References 2 and 3 should be consulted for a detailed
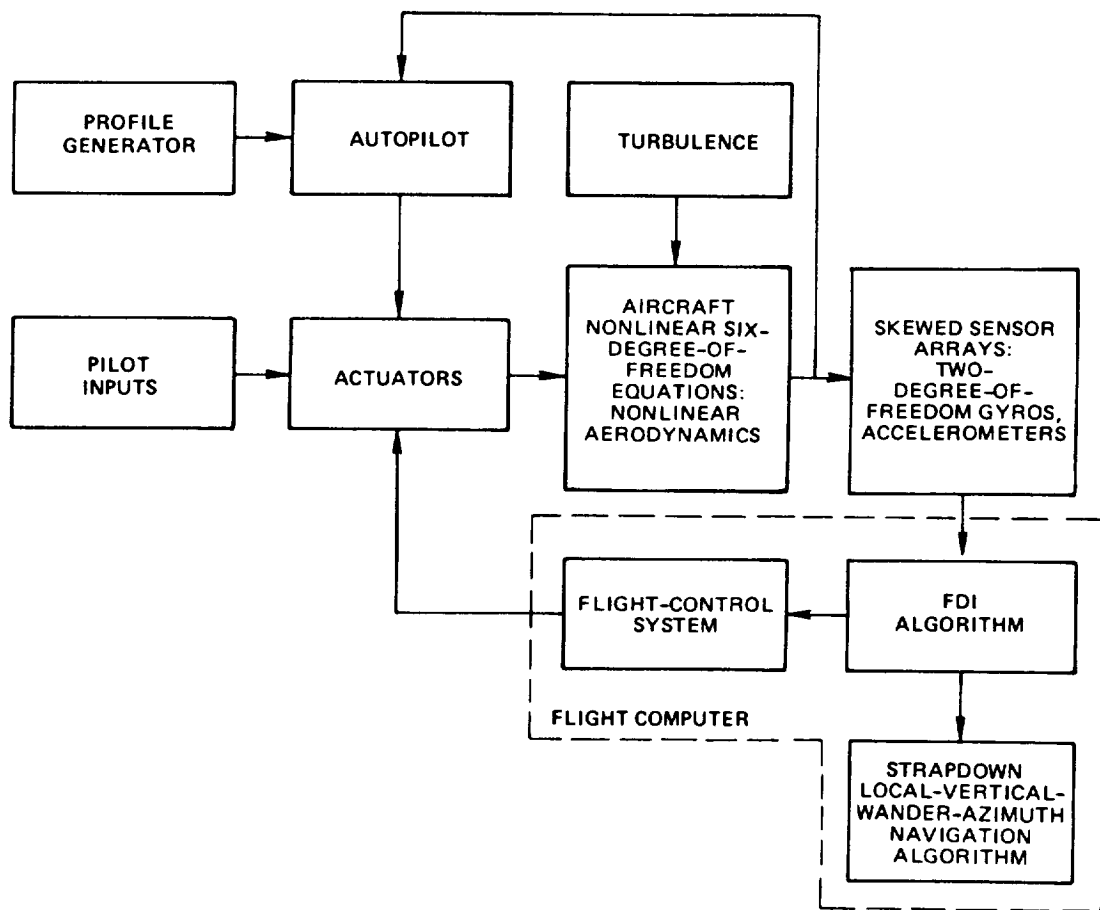

Figure 4. Simulation block diagram.

description of its components). The core of the simulation is a six-degree-of-freedom aircraft model with nonlinear aerodynamics. Also modeled are a flight-control system and turbulence. An autopilot "commands" the vehicle to follow a desired trajectory profile. Skewed gyro and accelerometer sensor configurations are modeled with the location of the sensors variable to permit an assessment of accelerometer lever-arm effects. The sensors are assumed to be of navigation quality and used for navigation and flight-control purposes. The FDI algorithm operates on the sensor data to generate the input signals to the flight-control and navigation systems. Navigation accuracy is assessed by differencing the outputs of a strapdown local-vertical-wander-azimuth navigation system model and the vehicle states.

SECTION 4

INSTRUMENT MODELS AND FAILURE MODES

The instrument models contained in the simulation[2,3] are generic
in nature, with their parameters selected to provide a state-of-the-art
level of performance. The TDOF gyro models include the effects of mis-
alignment, bias, quantization, g, g×g, ω×ω and scale-factor errors, and
a lag. The accelerometer models include errors due to misalignment,
lag, bias, input-pendulous-axis cross-coupling, quantization, and scale-
factor linear and nonlinear effects. Tables 1 and 2 give the nominal
set of sensor parameters.[4] The sensor error parameters are assumed
to be Gaussian distributed zero-mean random variables with 1σ values
equal to their nominal values. Block diagrams of the sensor models are
shown in Figures 5, 6, and 7 to illustrate the computations performed,
errors included, and the information flow. Only one axis of the TDOF
gyro is shown in Figures 6 and 7. A similar expression holds for the
other axis; the same TDOF error effects are applicable to both axes.
A further assumption is made regarding the error parameters of the TDOF
instruments used in this study. Based on the data presented in Refer-
ence 4, it is assumed that $\delta_{g_{j2}} = \delta_{g_{j3}} = 0.0$. This assumption can
be modified to reflect the values of the actual instruments to be im-
plemented in the IMU.

Failure modes of TDOF instruments may be either single-degree-of-
freedom (SDOF) or TDOF in nature. An SDOF failure may be caused by any
part of the rebalance loop on a given axis (including software). The

10

Table 1. Two-degree-of-freedom gyro nominal parameters.

Parameter	Value
Scale Factor	1/1.57 pulses/sec
Bias	0.01°/h
Scale-Factor Error	20 ppm
Misalignment Coefficients	50 μrad
g-Dependent Errors	0.005°/h/g
g^2, g×g-Dependent Errors	$0.02°/h/g^2$
ω×ω-Dependent Errors	$12.4°/h/(rad/s)^2$
Time Constant of Lag	0.003 s

Table 2. Accelerometer nominal parameters.

Parameter	Value
Scale Factor	3280.8 pulses/m/s (1000 pulses/ft/s)
Bias	50 μg
Scale-Factor Error	50 ppm
Misalignment Coefficients	50 μrad
Input-Pendulous Axes Acceleration Sensitivity Coefficient	$70 μg/g^2$
Input-Axis Acceleration-Squared Sensitivity Coefficients	$20 μg/g^2$
Time Constant of Lag	0.0002 s
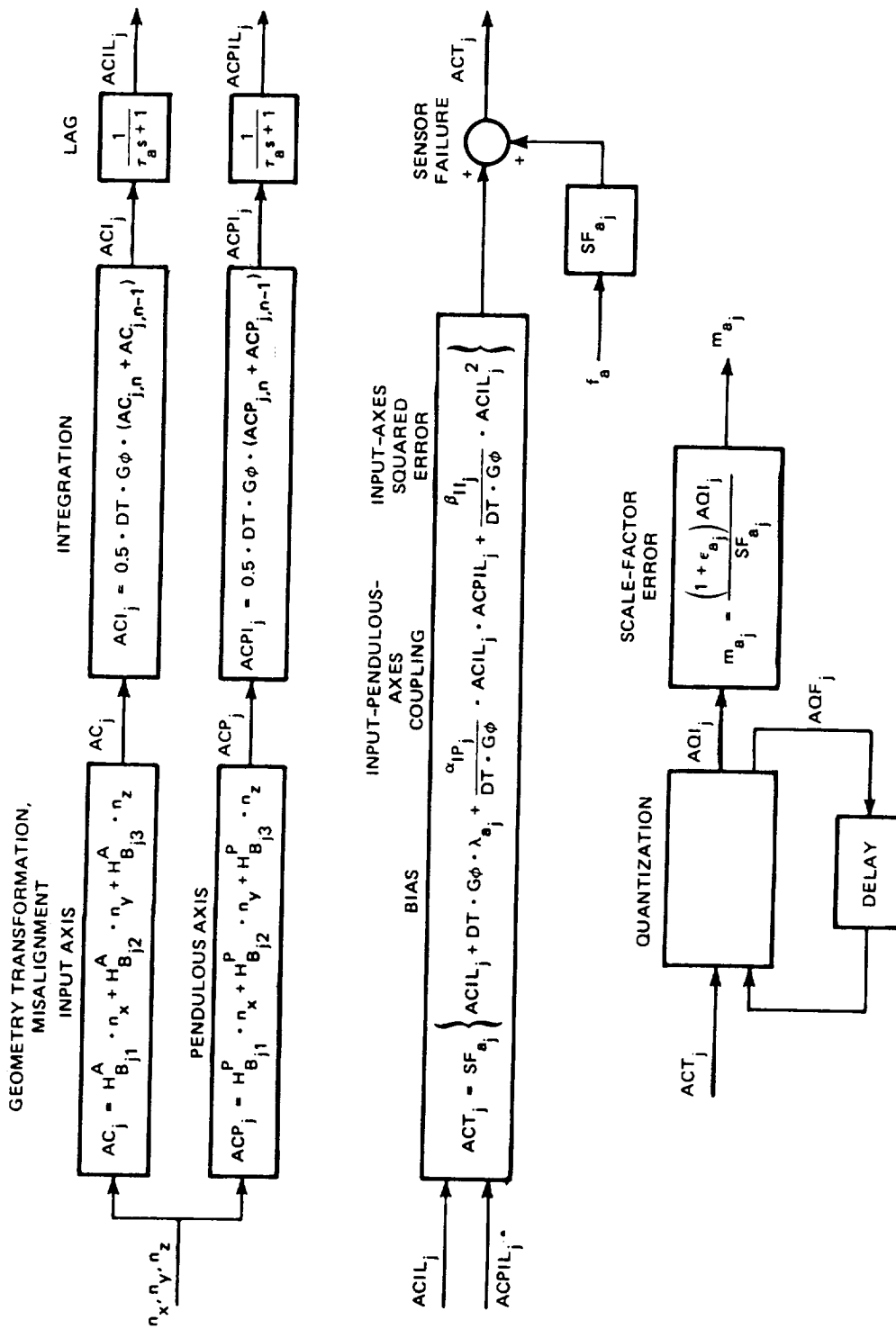
Figure 5.   Accelerometer model.

12

GEOMETRY TRANSFORMATION, MISALIGNMENT

$$GY_j = H^G_{B_{j1}} \cdot p + H^G_{B_{j2}} \cdot q + H^G_{B_{j3}} \cdot r$$

INTEGRATION

$$GYI_j = 0.5 \cdot DT \cdot DTR \cdot \left(GY_{j,n} + GY_{j,n-1}\right)$$

p, q, r

GY_j

GYI_j

BIAS   TDOF
           EFFECTS

$$GCT_j = SF_{g_j}\left(GYI_j + DT \cdot DTR \cdot \lambda_{g_j} + TDF_j\right)$$

GYI_j

TDF_j
(Figure 7)

SENSOR
FAILURE

$$+ \quad + $$

GCT_j

SF_{g_j}

f_g

LAG

$$\frac{1}{\tau_g s + 1}$$

QUANTIZATION

SCALE-FACTOR
ERROR

$$m_{g_j} = \frac{\left(1 + \epsilon_{g_j}\right) GQI_j}{SF_{g_j}}$$

GCT_j

$GCTL_j$

GQI_j

m_{g_j}

DELAY

GQF_j

Figure 6. Gyro model.

TDOF ERRORS

$$TDF_j = \frac{DTR}{G\phi} \cdot \left\{ \delta_{g_{j1}} \cdot AGYl_j + \delta_{g_{j2}} \cdot AGYl_{jk} \right.$$
$$\left. + \delta_{g_{j3}} \cdot AGYl_{jk} \right\}$$

$$+ \frac{DTR}{(DT \cdot G\phi^2)} \left\{ \delta_{g_{j4}} \cdot AGYl_j^2 \right.$$
$$+ \delta_{g_{j6}} \cdot AGYl_{jk}^2$$
$$+ \delta_{g_{j7}} \cdot AGYl_j \cdot AGYl_k$$
$$+ \delta_{g_{j8}} \cdot AGYl_k \cdot AGYl_{jk}$$
$$\left. + \delta_{g_{j9}} \cdot AGYl_j \cdot AGYl_{jk} \right\}$$

$$+ \frac{DTR}{DT} \left\{ \delta_{n_{j8}} \cdot GYl_k \cdot GYl_{jk} \right.$$
$$\left. + \delta_{n_{j9}} \cdot GYl_j \cdot GYl_{jk} \right\}$$

$\longrightarrow TDF_j$ (Figure 6)

INTEGRATION

$AGYl_j = 0.5 \cdot DT \cdot G\phi \cdot (AGY_{j,n} + AGY_{j,n-1})$

$AGYl_k = 0.5 \cdot DT \cdot G\phi \cdot (AGY_{k,n} + AGY_{k,n-1})$

$AGYl_{jk} = 0.5 \cdot DT \cdot G\phi \cdot (AGYl_{jk,n} + AGYl_{jk,n-1})$

$GYl_{jk} = 0.5 \cdot DT \cdot DTR \cdot (GY_{jk,n} + GY_{jk,n-1})$

ACCELERATIONS

FIRST GYRO INPUT AXIS

$AGY_j = H^G_{B_{j1}} \cdot n_x + H^G_{B_{j2}} \cdot n_y + H^G_{B_{j3}} \cdot n_z$

SECOND GYRO INPUT AXIS

$AGY_k = H^G_{B_{k1}} \cdot n_x + H^G_{B_{k2}} \cdot n_y + H^G_{B_{k3}} \cdot n_z$

SPIN AXIS

$AGY_{jk} = H^S_{B_{jk1}} \cdot n_x + H^S_{B_{jk2}} \cdot n_y + H^S_{B_{jk3}} \cdot n_z$

ANGULAR-RATE SPIN AXIS

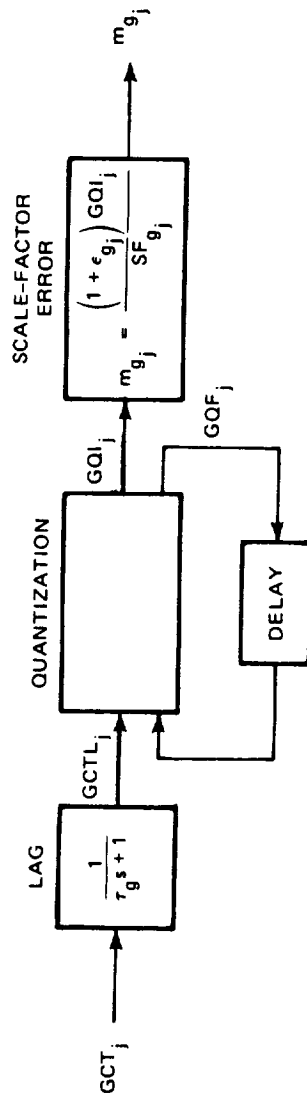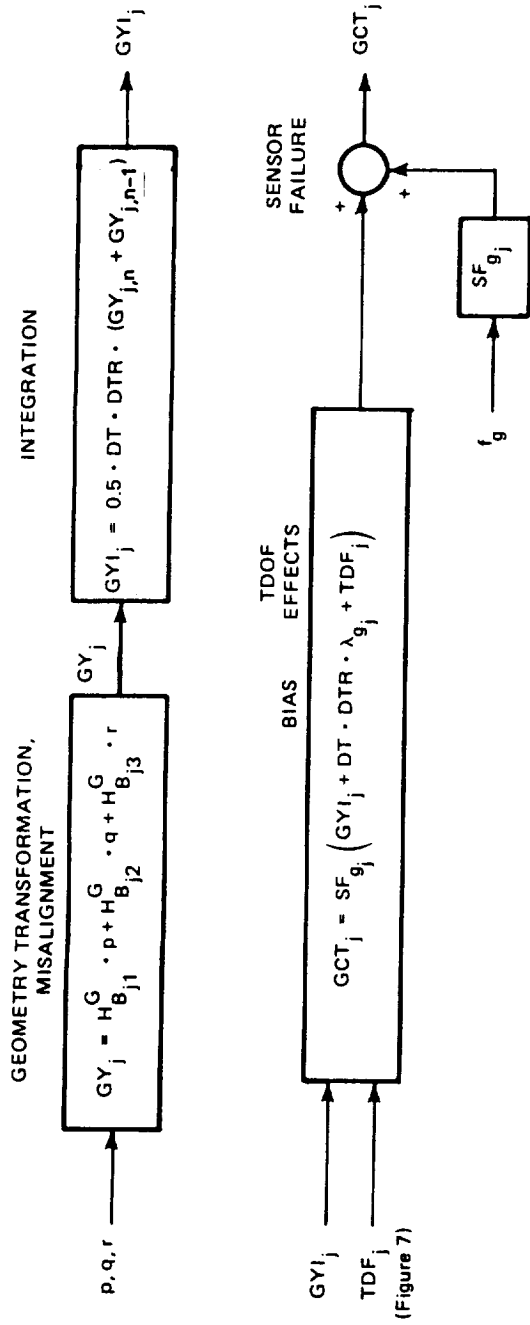$GY_{jk} = H^S_{B_{jk1}} \cdot p + H^S_{B_{jk2}} \cdot q + H^S_{B_{jk3}} \cdot r$
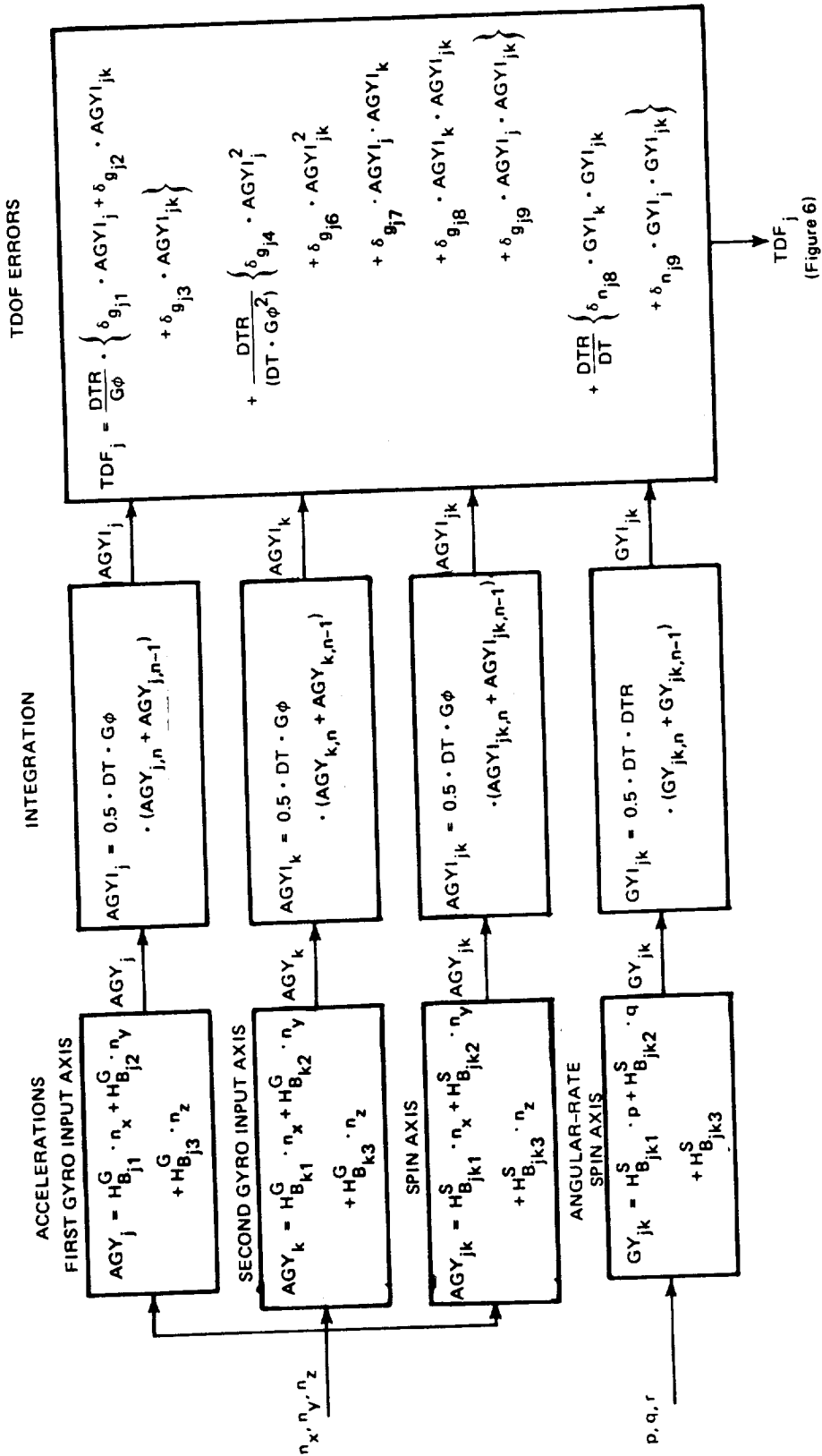
n_x, n_y, n_z

p, q, r

Figure 7. TDOF gyro errors.

14

high degree of correlation or coupling between the axes, caused by the common wheel or pendulum, will propagate the failure into the second axis in a short time. Therefore, when a failure is isolated, an entire sensor is removed, regardless of the character of the failure.

Experience with dry TDOF instruments as a class indicates that small performance shifts (such as bias changes turn-on to turn-on) are the rule. Parameter shifts of larger magnitude are found only as catastrophic failures (such as wheel bearing or rebalance-loop failures). Such failures, then, will be on the same order of magnitude as the inputs.

SECTION 5

EVALUATION TRAJECTORY

.

Figure 8 shows the 1-hour flight profile used to evaluate the
fault-tolerant system during the dynamic phases of the vehicle flight.
The profile includes features from a typical transport aircraft mission
profile: a climb to altitude, cruise, heading changes, descent, and a
loiter maneuver. Table 3 gives the details of the evaluation flight
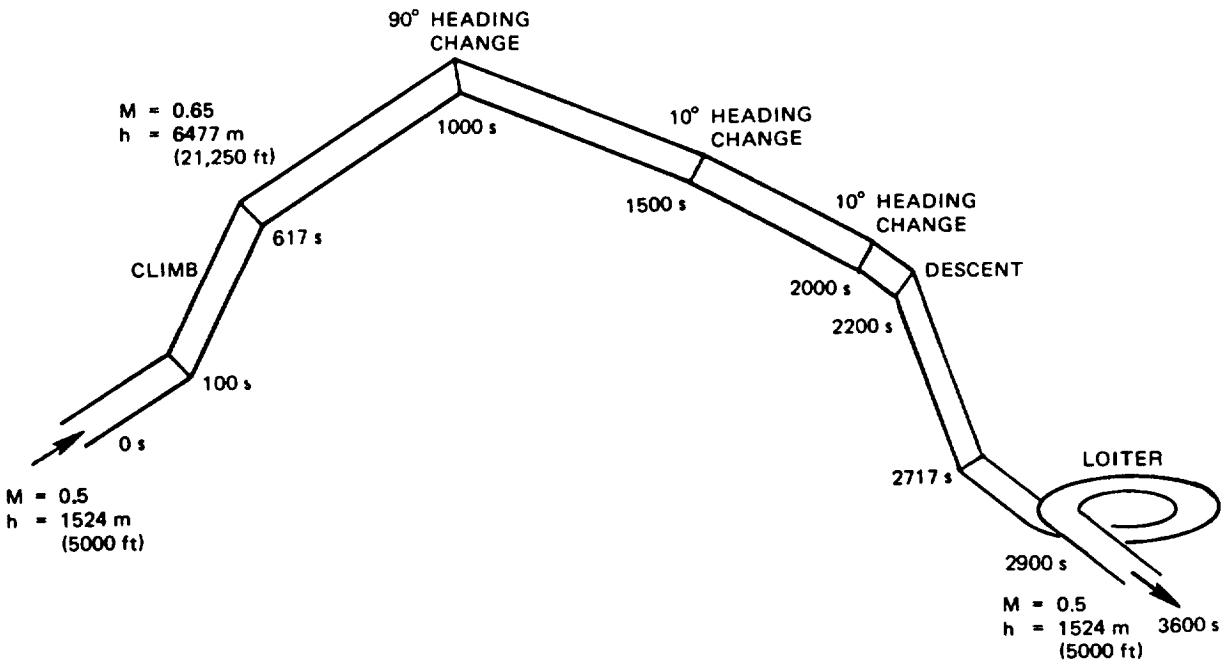trajectory.

Figure 8. Evaluation trajectory profile.

Table 3. Evaluation trajectory description.

Time (s)	Event	Altitude (m)	Mach Number
0 - 100	Cruise	1,524 (5,000 ft)	0.5
100 - 617	Ascent		
617 - 1,000	Cruise	6,477 (21,250 ft)	0.653
1,000 - 1,090	90° heading change		
1,090 - 1,500	Cruise	6,477 (21,250 ft)	0.653
1,500 - 1,510	10° heading change		
1,510 - 2,000	Cruise	6,477 (21,250 ft)	0.653
2,000 - 2,010	10° heading change		
2,010 - 2,200	Cruise	6,477 (21,250 ft)	0.653
2,200 - 2,717	Descent		
2,717 - 2,900	Cruise	1,524 (5,000 ft)	0.5
2,900 - 3,340	Loiter; one 360° turn		
3,340 - 3,600	Cruise	1,524 (5,000 ft)	0.5

The vehicle responses, as well as other system responses obtained from the simulation using this trajectory, are presented in Figure 9 to give an indication of how well the vehicle follows the commanded trajectory and to show the magnitude of important rates and accelerations obtained during the course of the mission. The trajectory commands are also presented in this figure, as are the north and east ground velocities and latitude and longitude of the vehicle during the trajectory. A nominal gust intensity of 1.83 meters (6 feet) per second was selected.
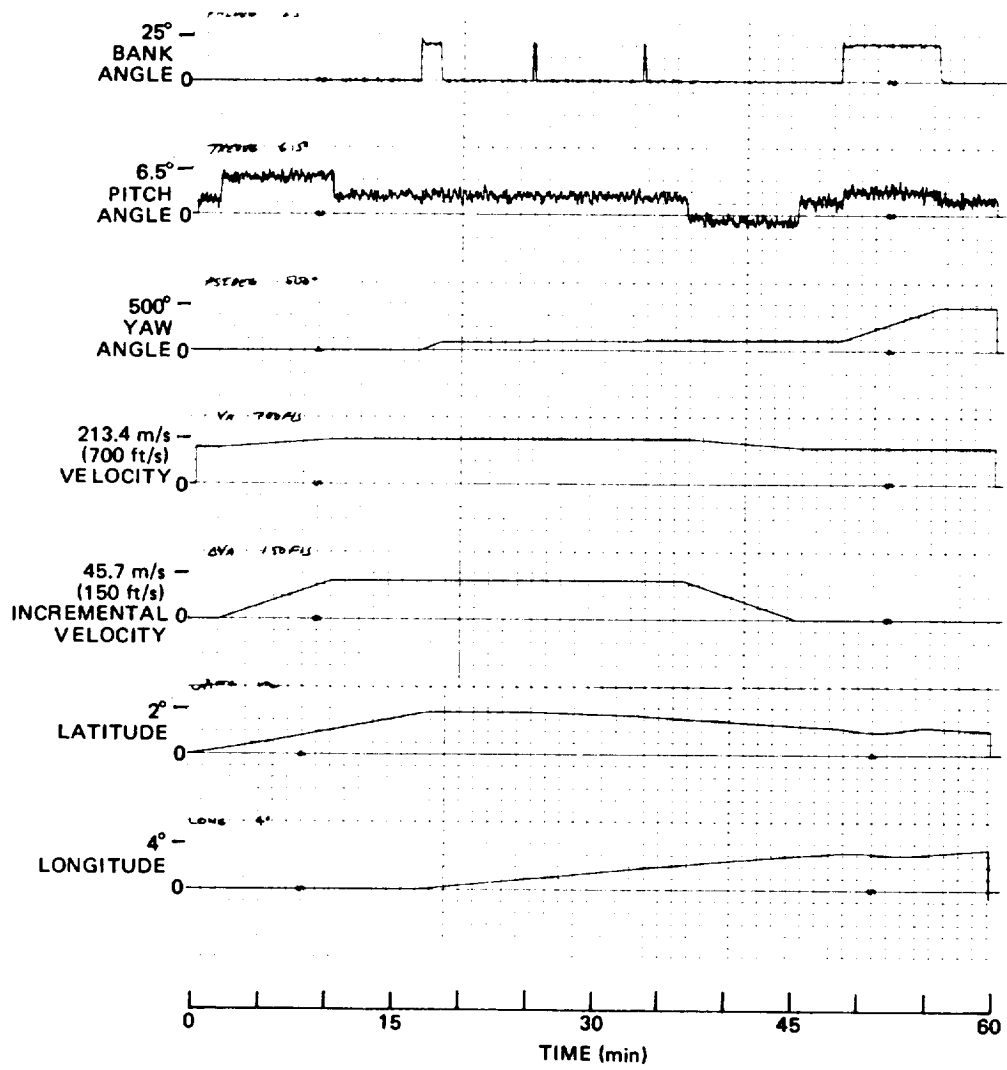
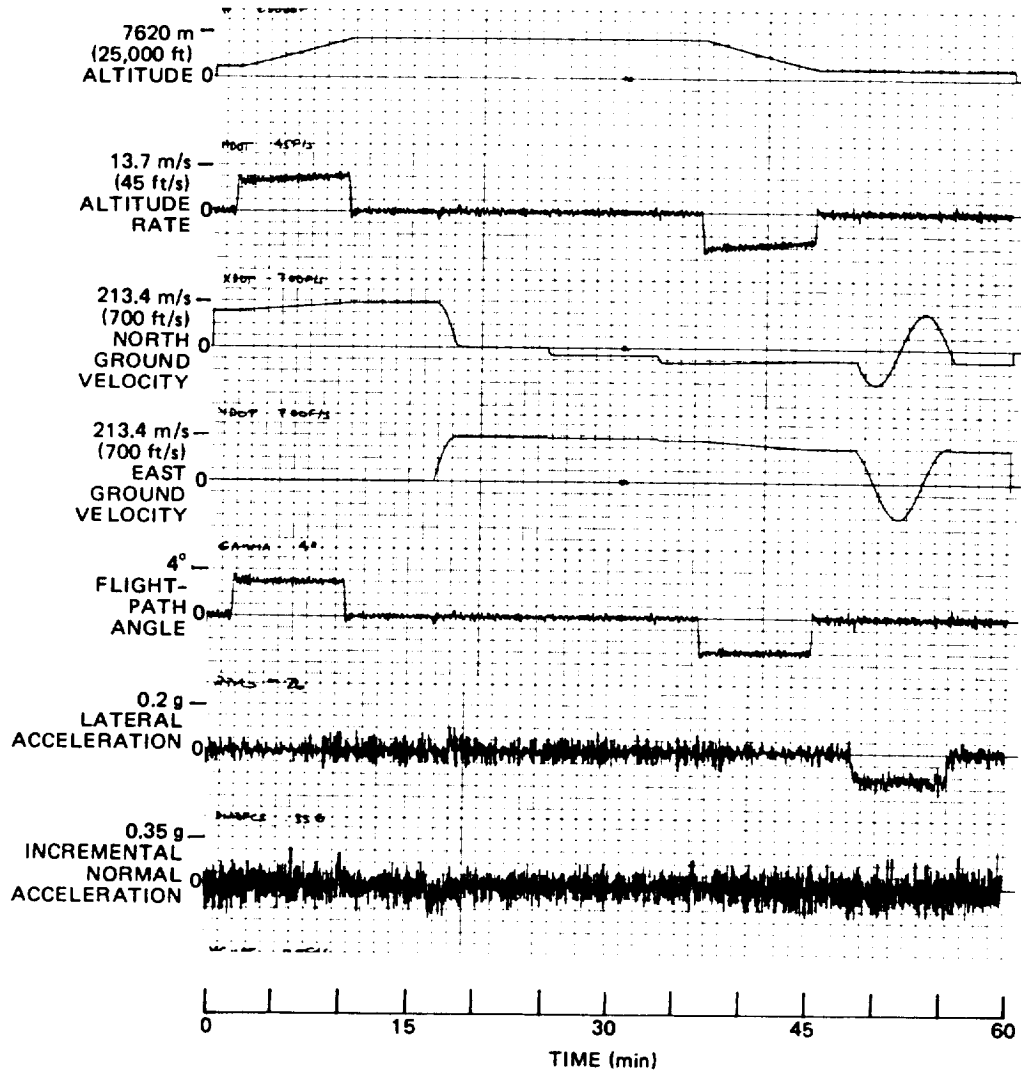Figure 9. System responses obtained for the dynamic trajectory (sheet 1 of 4).

18

Figure 9.   System responses obtained for the dynamic trajectory
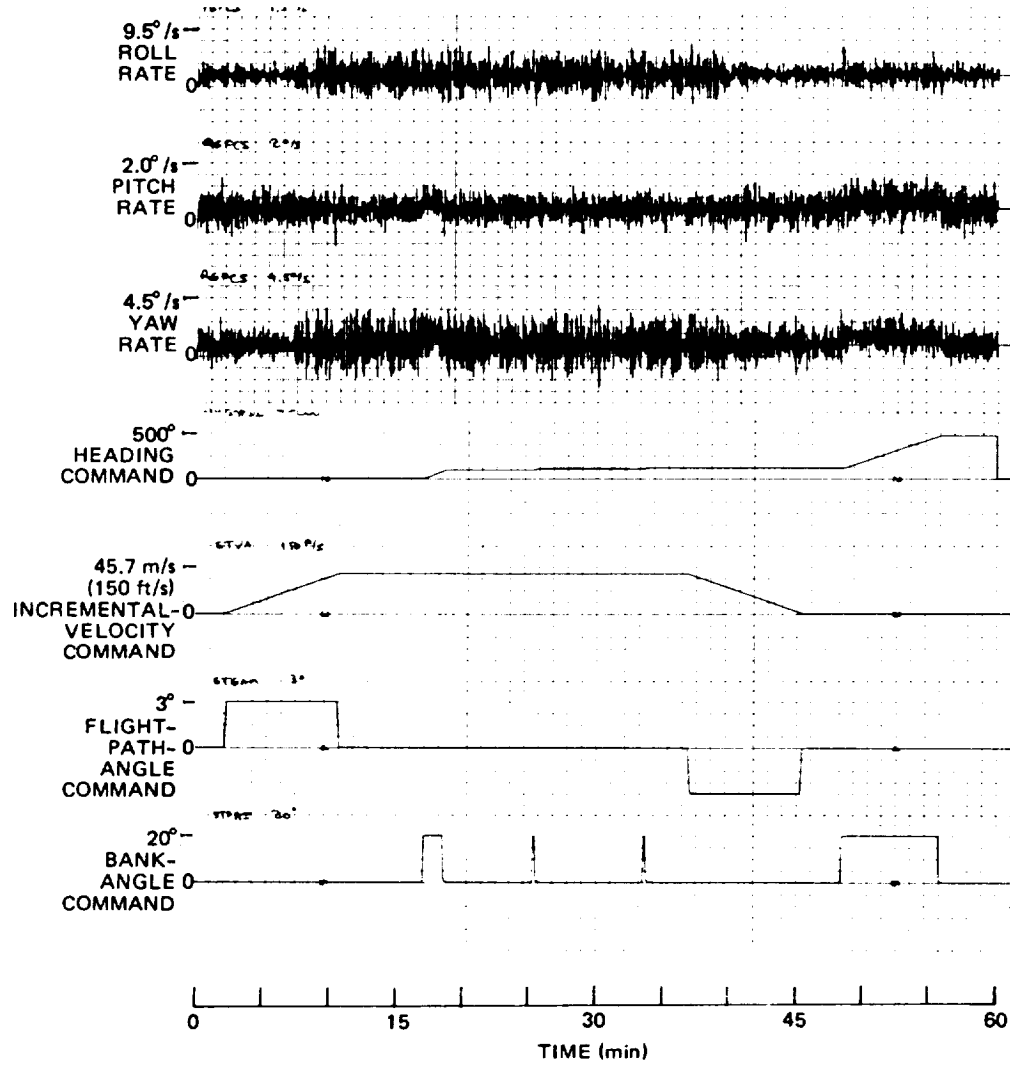(sheet 2 of 4).

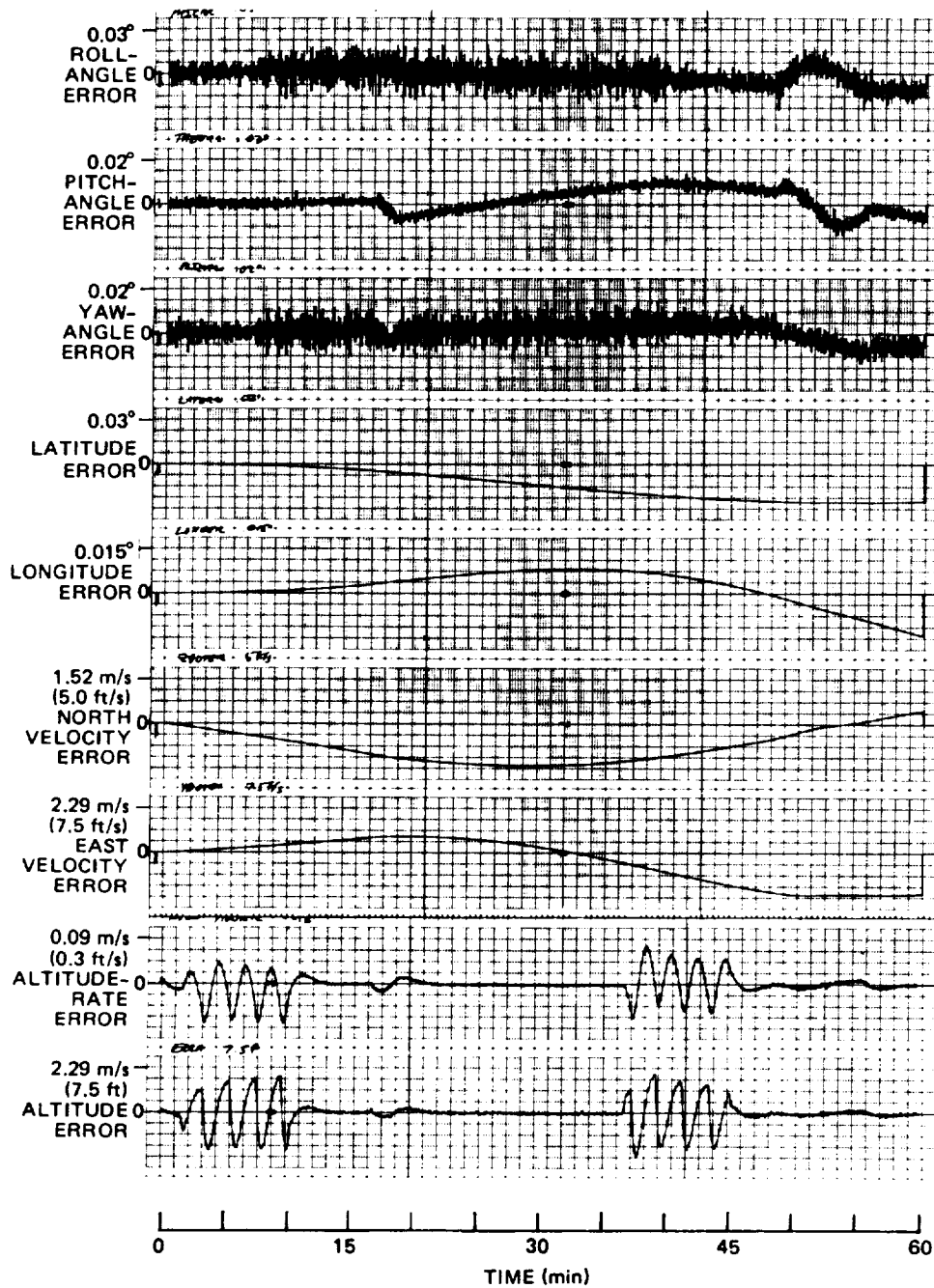Figure 9. System responses obtained for the dynamic trajectory (sheet 3 of 4).

Figure 9. System responses obtained for the dynamic trajectory (sheet 4 of 4).

21

As indicated in Figure 9, the vehicle is initially trimmed at an altitude (h) of 1,524 meters (5,000 feet) and speed of mach (M) = 0.5. After a 100-second cruise at this flight condition, the vehicle begins to climb and continues climbing for 517 seconds until it reaches an altitude of 6,477 meters (21,250 feet) and a speed of M = 0.65. The flight-path angle of the vehicle is 3 degrees and the rate of ascent 609.6 meters (2,000 feet) per minute. The vehicle then cruises until 1,000 seconds into the mission, at which time a heading change of 90 degrees is commanded. The vehicle banks at 20 degrees, its nominal roll rate is 4.4 degrees per second, and its turn rate is approximately 1 degree per second. Another period of cruising flight follows which is interrupted by two 10-degree heading changes: one at 1,500 seconds and one at 2,000 seconds. The vehicle's bank angle, roll rate, and turn rate are the same as for the 90-degree heading change. At 2,200 seconds, the vehicle begins a descent to an altitude of 1,524 meters (5,000 feet) and M = 0.5. The rate of descent is 609.6 meters (2,000 feet) per minute, and the flight-path angle is -3 degrees. The vehicle then cruises at this flight condition until 2,900 seconds, at which time one 360-degree turn is commanded to simulate a loiter maneuver. Significant vehicle parameters during the loiter are: a bank angle of 20 degrees, a roll rate of approximately 4 degrees per second, and a turn rate of 0.75 degree per second. At the end of the loiter, the vehicle cruises to complete the 1-hour trajectory.

The navigation errors obtained with a randomly selected set of sensor errors for the redundant IMU are also presented in Figure 9. The position errors are in the 1.85- to 3.70-kilometer- (1- to 2-nautical-mile-) range, while the velocity errors are less than 2.29 meters (7.5 feet) per second.

SECTION 6

THE FDI SYSTEM

Figure 10[5] is a block diagram of the baseline FDI system. The system shown here is mechanized to detect and isolate three levels of failure:

(1)   Hard failures: those of a comparatively large magnitude, which primarily affect flight-control performance.

(2)   Midvalue failures: those of medium magnitude, which affect pilot display performance.

(3)   Soft failures: those of a comparatively small magnitude, which affect navigation performance.

The major emphasis of this study was on the detection and isolation of soft failures. Built-in-test-equipment (BITE) processing was not considered during this study, but indications are that it will be necessary to detect simultaneous multiple failures.

The detection and isolation of sensor failures is accomplished by processing the sensor outputs via a set of parity equations. The parity equations are linear, constant-coefficient equations selected to remove from the data the effect of the quantity which the sensors are measuring. That is, the angular-rate information is removed from the gyro outputs and the acceleration information is removed from the accelerometer outputs. Only the effects of the uncertainties associated with the sensors remain as parity-equation residuals. The parity-equation residuals are then used to ascertain the presence or absence of a failure.

Two techniques are explored in this study for detecting the presence of a failure: the Edge Vector Test (EVT)[1] and the Generalized Likelihood Test (GLT).[6-8]
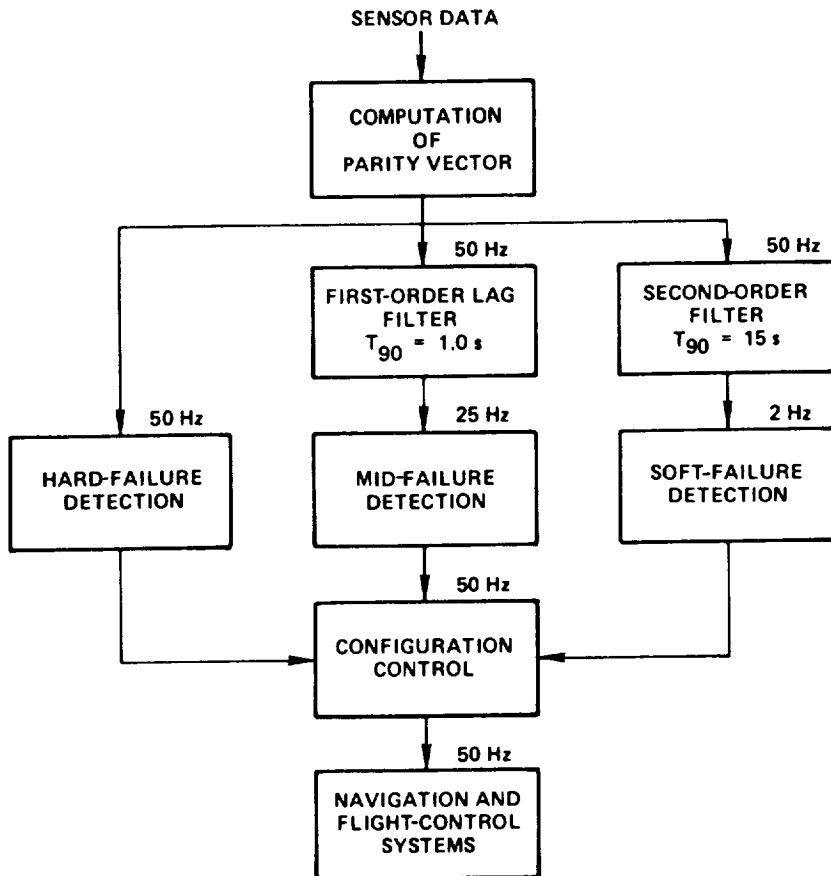

Figure 10. FDI algorithm block diagram.

The parity-equation residuals are a function of the sensor errors, sensor noise, etc., and the effect of the aircraft flight environment on these uncertainties. When there is no failed sensor present, these uncertainties define a baseline of FDI system operation. When a sensor failure occurs, the value and statistics of the parity-equation residuals change to reflect the presence of this failure. For example, a large bias failure causes a step increase in the parity-equation residuals at

the time of the sensor failure. A failure is detected when the parity-equation residuals or a function of them exceeds a certain threshold. The selection of the proper thresholds is a significant part of the design of an FDI system. The basic problem is to select thresholds which allow the detection and isolation of the smallest possible failures, ensuring the best possible system performance while minimizing the probability of the false detection of sensor failures due to sensor noise, quantization, etc. Furthermore, the effects of the vehicle trajectory and the maneuvers associated with it may require dynamic failure-detection thresholds since the nominal values of the FDI system parity-equation residuals are larger when the vehicle undergoes dynamic maneuvers.

Because they are of a large magnitude, hard failures are detected using the raw sensor data and parity-equation residuals. A hard-failed sensor must be removed immediately from the system to ensure a safe flight. As the presence of less significant failures may be masked in the raw sensor data or parity-equation residuals by the nominal sensor errors and, in particular, by high-frequency sensor noise, quantization, etc., the parity-equation residuals are low-pass filtered to increase the ratio of the sensor failure effect to the sensor noise and quantization effects. For the mid- and soft-failure channels, the detection and isolation of a failure is achieved in the same manner as with the hard-failure channel, except that the filtered parity-equation residuals are used.

To detect moderate or midvalue failures, a first-order lag with a fairly fast response is used. These failures are also of a large enough magnitude that it is desirable to remove them as quickly as possible so that system performance is not compromised. Heavier filtering, to decrease the sensor background noise level even further, is used to detect the smaller soft failures, as they can be tolerated for a longer time before major disturbances to system performance show up. For the baseline FDI system, the filter associated with the midvalue-failure channel is a first-order lag with a time constant of 0.434 second (rise

25

time to 90-percent response, $T_{90} = 1.0$ second). The filter associated with the soft-failure channel is a second-order system (two first-order lags in series) with $T_{90} = 15$ seconds. No significant benefits are gained from the use of filters beyond second order.[9,10]

FDI of the hard failures is performed at the sensor computation rate, i.e., 50 Hz in this case. This is done so that the output data from a hard-failed sensor can be disregarded before it can affect the controllability of the air vehicle. The sampling rate for the mid- and soft-failure channels can be done at a lower rate since the flight controllability of the vehicle is not an issue for failures of these magnitudes. The actual sampling rates used are not especially critical, and the only requirement is that they be fast enough to be consistent with the desired system performance; the mid-failure-channel sampling rate should be faster than that of the soft-failure channel because larger failures are being detected. Rates of 25 and 2 Hz were used for the mid- and soft-failure channels, respectively.

It should be emphasized that because of the TDOF instruments in this system, when a failure is isolated an entire sensor is removed even if only a single-axis failure is detected. This ensures that the second axis of a sensor, whose performance is highly correlated with the other axis, will not degrade system performance.

SECTION 7

THRESHOLD SELECTION

The technique used to deal with the problem of detecting faults at acceptably low levels, while accommodating the effects of maneuvering flight, was to implement thresholds composed of both constant and dynamic quantities. The constant portion was included to account for the effects of quantization and sensor noise during straight and level flight, while the dynamic portion accounts for the effects due to maneuvering flight.

The approach implemented for computing the dynamic FDI thresholds analytically duplicates the calculation of the failure-decision functions using a derived expression for the upper bound of the sensor errors and parity-equation residuals. Figure 11 illustrates the procedure. Quantization effects and sensor noise are neglected as they are not easily
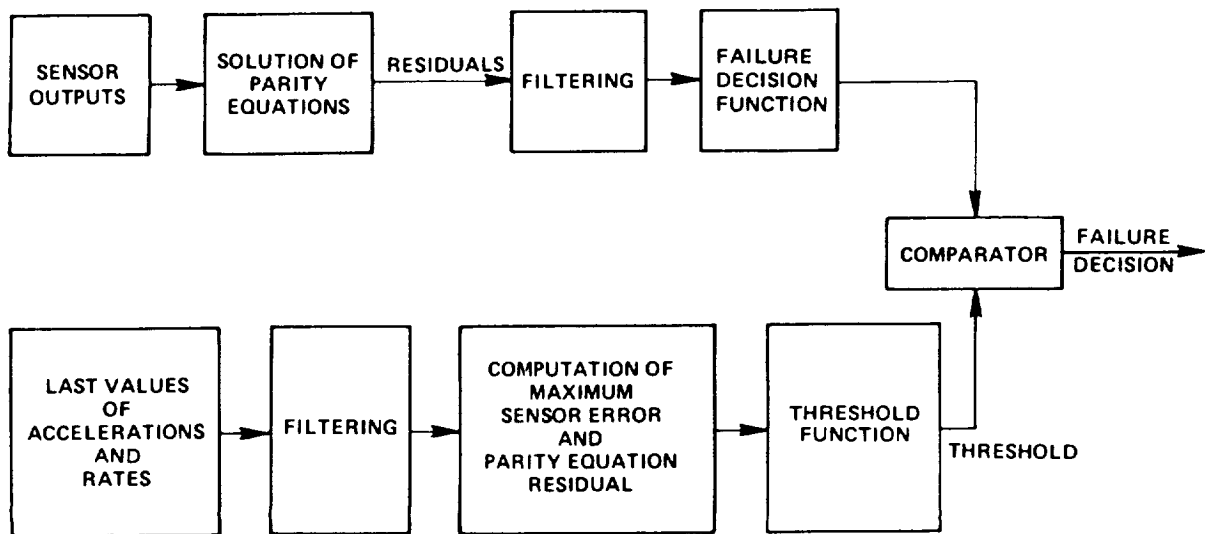

Figure 11. Computation of dynamic thresholds.

27

defined analytically and they are accounted for with the constant portion of the threshold function. Furthermore, the filtering of the parity-equation residuals attenuates the effects of quantization and sensor noise, and the sensor error effects predominate during dynamic flight phases.

The derived expression used for the upper bound of the sensor errors and parity-equation residuals is a function of the sensor error model, the magnitude of the sensor errors, and the body-axes linear accelerations and angular rates. The 3σ values of the sensor errors can be used to develop a system suitable for operation with most sensors of the type to be included in this system. However, these values can be adjusted to achieve desired probabilities of false-alarm detection, etc. The last-pass values of the body-axes linear accelerations or angular rates calculated for the flight-control system are used in the generation of the dynamic thresholds.

The angular rates and linear accelerations are filtered before computation of the maximum sensor error and parity-equation residual for the mid- and soft-failure channels. This reduces the noise level of the signals caused by turbulence, sensor noise, etc., and results in acceptable threshold levels for the detection of soft failures. Strictly speaking, the sensor outputs should be filtered before the parity equations are solved. However, the parity equations are linear, and the solution of the parity equations and the filtering operations are interchangeable. It is more efficient to filter the parity-equation residuals since fewer filters are required.

SECTION 8

THE EDGE VECTOR TEST (EVT)

8.1 Derivation

The parity equations and FDI algorithm for the redundant IMU are derived in this section using an edge equation formulation. This formulation is based on the projection of rates (or accelerations) measured in two planes along the line of intersection of the planes. As the measurement planes are orthogonal to the spin (or pendulous) axes, the "edge vectors" are defined by the line mutually perpendicular to these axes. For measurement planes i,j (j > i)

$$\hat{e}_{ij} \; = \; \text{UNIT} \; (\hat{s}_i \times \hat{s}_j) \; = \; \frac{\hat{s}_i \times \hat{s}_j}{|\hat{s}_i \times \hat{s}_j|}$$

For the geometry shown in Figure 2, $\hat{e}_{ij}$ may be tabulated as

$$\hat{e}_{12} \; = \; \frac{1}{\sqrt{2}} \begin{bmatrix} 0 \\ -1 \\ 1 \end{bmatrix} \qquad \hat{e}_{13} \; = \; \frac{1}{\sqrt{2}} \begin{bmatrix} 1 \\ -1 \\ 0 \end{bmatrix} \qquad \hat{e}_{14} \; = \; \frac{1}{\sqrt{2}} \begin{bmatrix} 1 \\ 0 \\ -1 \end{bmatrix}$$

$$\hat{e}_{23} \; = \; \frac{1}{\sqrt{2}} \begin{bmatrix} 1 \\ 0 \\ 1 \end{bmatrix} \qquad \hat{e}_{24} \; = \; \frac{1}{\sqrt{2}} \begin{bmatrix} 1 \\ 1 \\ 0 \end{bmatrix} \qquad \hat{e}_{34} \; = \; \frac{1}{\sqrt{2}} \begin{bmatrix} 0 \\ 1 \\ 1 \end{bmatrix}$$

where the $\hat{e}_{ij}$ are in body-frame coordinates.

Rates (accelerations) measured in the i and j planes may be compared if they are expressed in a common frame. The frame chosen here is, again, the body frame. Then the residual R_{ij} may be expressed by

$$R_{ij} = (\hat{\omega}_i^B - \hat{\omega}_j^B) \cdot \hat{e}_{ij}^B \qquad (1)$$

If $|R_{ij}| > T$, an FDI threshold, then a miscompare flag, F_{ij}, is set. FDI consists of logical operations on the flags F_{ij}.

Equation (1) is written in terms of $\hat{\omega}_i^B$, the measurement vector from the ith plane transformed into body coordinates. In response to a body rate (specific force) $\hat{\omega}_B^B$, the ith measurement in the gyro frame will be

$$\hat{\omega}_i^G = \begin{bmatrix} \hat{H}_{B_{i1}}^{G^T} \\ \\ \hat{H}_{B_{i2}}^{G^T} \\ \\ \hat{0}^T \end{bmatrix} \hat{\omega}_B^B + \begin{bmatrix} \zeta_{i1} \\ \\ \zeta_{i2} \\ \\ 0 \end{bmatrix}$$

where $\hat{H}_{B_{ik}}^G$ are the corresponding rows of the matrix $\hat{H}_B^G$, and the ζ's are uncertainties in the measurements, i.e., noise, sensor-error effects, failure effects, etc. Independence of the components of ζ may not be assumed because of the high correlation of the failure modes of TDOF instruments.

$\hat{\omega}_i^G$ is expressed in body coordinates by

$$\hat{\omega}_i^B = \begin{bmatrix} \hat{H}_{B_{i1}}^G & | & \hat{H}_{B_{i2}}^G & | & \hat{H}_{B_i}^S \end{bmatrix} \hat{\omega}_i^G$$

where, again, $\hat{\omega}_i^G = [\omega_{i1}, \omega_{i2}, 0]$ and ω_{i1}, ω_{i2} are the compensated $\Delta\theta$ or ΔV measurements in the ith plane.

For example, consider the $i,j = 1,2$ measurement pair. In response to an input $\hat{\omega}_B^B = [\omega_x, \omega_y, \omega_z]^T$, we find

$$
\hat{\omega}_1^G = \frac{1}{2\sqrt{3}}
\begin{bmatrix}
\bar{b}\omega_x - \bar{a}\omega_y + 2\omega_z \\
-\bar{a}\omega_x + \bar{b}\omega_y + 2\omega_z \\
0
\end{bmatrix}
+
\begin{bmatrix}
\zeta_{11} \\
\zeta_{12} \\
0
\end{bmatrix}
$$

$$
= \frac{1}{2\sqrt{3}}
\begin{bmatrix}
\bar{b}\omega_x - \bar{a}\omega_y + 2\omega_z + E_{11} \\
-\bar{a}\omega_x + \bar{b}\omega_y + 2\omega_z + E_{12} \\
0
\end{bmatrix}
$$

where

$$
\bar{a} = \sqrt{3} + 1
$$

$$
\bar{b} = \sqrt{3} - 1
$$

$$
E_{ij} = 2\sqrt{3}\,\zeta_{ij}
$$

Similarly

$$
\hat{\omega}_2^G = \frac{1}{2\sqrt{3}}
\begin{bmatrix}
\bar{a}\omega_x + \bar{b}\omega_y + 2\omega_z + E_{21} \\
-\bar{b}\omega_x - \bar{a}\omega_y + 2\omega_z + E_{22} \\
0
\end{bmatrix}
$$

Given the measurements $\hat{\omega}_1^G$, $\hat{\omega}_2^G$ in the coordinates of their respective frames, the data are transformed to the common body frame by

31

$$\hat{H}^B_{G_i} = \left[\hat{H}^G_{B_{i1}} \;\vdots\; \hat{H}^G_{B_{i2}} \;\vdots\; \hat{H}^S_{B_i} \right]$$

$$\hat{H}^B_{G_1} = \frac{1}{2\sqrt{3}} \begin{bmatrix} \bar{b} & -\bar{a} & -2 \\ -a & \bar{b} & -2 \\ 2 & 2 & -2 \end{bmatrix}$$

$$\hat{H}^B_{G_2} = \frac{1}{2\sqrt{3}} \begin{bmatrix} \bar{a} & -\bar{b} & 2 \\ \bar{b} & -\bar{a} & -2 \\ 2 & 2 & -2 \end{bmatrix}$$

and

$$\hat{\omega}^B_1 = \frac{1}{12} \begin{bmatrix} 8\omega_x - 4\omega_y - 4\omega_z + \bar{b}E_{11} - \bar{a}E_{12} \\ -4\omega_x + 8\omega_y - 4\omega_z - \bar{a}E_{11} + \bar{b}E_{12} \\ -4\omega_x - 4\omega_y + 8\omega_z + 2E_{11} + 2E_{12} \end{bmatrix}$$

$$\hat{\omega}^B_2 = \frac{1}{12} \begin{bmatrix} 8\omega_x + 4\omega_y + 4\omega_z + \bar{a}E_{21} - \bar{b}E_{22} \\ 4\omega_x + 8\omega_y - 4\omega_z + \bar{b}E_{21} - \bar{a}E_{22} \\ 4\omega_x - 4\omega_y + 8\omega_z + 2E_{21} + 2E_{22} \end{bmatrix}$$

Then

$$R_{12} = \left(\hat{\omega}^B_1 - \hat{\omega}^B_2 \right) \cdot \hat{e}^B_{12}$$

$$= \frac{1}{12\sqrt{2}} \begin{bmatrix} -8\omega_y - 8\omega_z + \bar{b}(E_{11} + E_{22}) - \bar{a}(E_{21} + E_{12}) \\ -8\omega_x + \bar{a}(E_{22} - E_{11}) + \bar{b}(E_{12} - E_{21}) \\ -8\omega_x + 2(E_{11} + E_{12} - E_{21} - E_{22}) \end{bmatrix} \cdot \begin{bmatrix} 0 \\ -1 \\ 1 \end{bmatrix}$$

$$= \frac{1}{12\sqrt{2}} \left[\sqrt{3}(E_{11} - E_{12} + E_{21} - E_{22}) + 3(E_{11} + E_{12} - E_{21} - E_{22}) \right]$$

$$= \frac{1}{2\sqrt{2}} \left[\bar{a}(\zeta_{11} - \zeta_{22}) + \bar{b}(\zeta_{12} - \zeta_{21}) \right]$$

R_{12} is independent of $\hat{\omega}^B_B$, the input; it is a function of only the uncompensated errors in the measurements. This is true in general for R_{ij}.

Each of the six residuals R_{ij}, $j > i$, represents a comparison of two instruments. If an instrument fails, the uncertainty vector associated with it has a nonzero bias and all residuals R_{ij} involving that instrument will be affected; any residual not involving that instrument will be unaffected. This provides a basis for a single-trial failure-isolation technique. Only n-3 or 5 independent parity equations exist for the redundant sensor configuration considered in this study. [6] Therefore, one of the six parity equations is a linear combination of the other five.

Assume a failure-isolation threshold, T, such that residuals exceeding T are deemed to represent failed instruments. Logical variables can be defined which indicate a pass (false) or fail (true) of a single paired comparison between the parity-equation residual and the threshold. Thus

$$\left| R_{ij} \right| > T \rightarrow F_{ij} = \text{true}$$

Logical operations over F_{ij} then isolate the failure.

In a practical application, the six parity equations are solved at the computation rate of the appropriate FDI channel. If fewer than two of the residuals exceed the threshold, failure isolation is not performed. This reduces the computational burden of the FDI system.

Consider instrument 1. Construct the logical equation

$$G_1 = (F_{12} \text{ and } F_{13}) \text{ or } (F_{12} \text{ and } F_{14}) \text{ or } (F_{13} \text{ and } F_{14})$$

If instrument 1 fails such that all of the residuals involving it exceed the threshold, all F_{1j} are true and G_1 is true. A similar equation for another instrument, say instrument 2, will be logically false, e.g.

$$G_2 = (F_{12} \text{ and } F_{23}) \text{ or } (F_{12} \text{ and } F_{24}) \text{ or } (F_{23} \text{ and } F_{34})$$

$$= (1 \cdot 0) + (1 \cdot 0) + (0 \cdot 0)$$

$$= 0 \text{ (false)}$$

The complete set of logical equations for four instruments is

$$G_1 = F_{12}F_{13} + F_{12}F_{14} + F_{13}F_{14}$$

$$G_2 = F_{12}F_{23} + F_{12}F_{24} + F_{23}F_{24}$$

$$G_3 = F_{13}F_{23} + F_{13}F_{34} + F_{23}F_{34}$$

$$G_4 = F_{14}F_{24} + F_{14}F_{34} + F_{24}F_{34}$$

To isolate a second failure, given instrument i has failed

$$G_j = F_{jk}F_{j\ell}$$

where i, j, k, ℓ is a cyclic permutation of 1, 2, 3, 4. That is

Instrument 1 Failed	Instrument 2 Failed	Instrument 3 Failed	Instrument 4 Failed
$G_2 = F_{23}F_{24}$	$G_1 = F_{13}F_{14}$	$G_1 = F_{12}F_{14}$	$G_1 = F_{12}F_{13}$
$G_3 = F_{23}F_{34}$	$G_3 = F_{13}F_{34}$	$G_2 = F_{12}F_{24}$	$G_2 = F_{12}F_{23}$
$G_4 = F_{24}F_{34}$	$G_4 = F_{14}F_{34}$	$G_4 = F_{14}F_{24}$	$G_3 = F_{13}F_{23}$

A third failure, given i,j failed, may be detected by noting that $F_{k\ell}$ is true, or that instruments k and ℓ miscompare.

The actual parity equations implemented in the simulation are in terms of the body-axes components of the sensed quantities. Thus, for the gyros the body-axes components of the sensed angular rates are

$$\omega^B_{1x} = 0.211325m_{g_{A1}} - 0.788675m_{g_{B1}}$$

$$\omega^B_{1y} = -0.788675m_{g_{A1}} + 0.211325m_{g_{B1}}$$

$$\omega^B_{1z} = 0.577350(m_{g_{A1}} + m_{g_{B1}})$$

$$\omega^B_{2x} = 0.788675m_{g_{A2}} - 0.211325m_{g_{B2}}$$

$$\omega^B_{2y} = 0.211325m_{g_{A2}} - 0.788675m_{g_{B2}}$$

$$\omega^B_{2z} = 0.577350(m_{g_{A2}} + m_{g_{B2}}) \tag{2}$$

$$\omega^B_{3x} = -0.211325m_{g_{A3}} + 0.788675m_{g_{B3}}$$

$$\omega^B_{3y} = 0.788675m_{g_{A3}} - 0.211325m_{g_{B3}}$$

$$\omega^B_{3z} = 0.577350(m_{g_{A3}} + m_{g_{B3}})$$

$$\omega^B_{4x} = -0.788675m_{g_{A4}} + 0.211325m_{g_{B4}}$$

$$\omega^B_{4y} = -0.211325m_{g_{A4}} + 0.788675m_{g_{B4}}$$

$$\omega^B_{4z} = 0.577350(m_{g_{A4}} + m_{g_{B4}}) \qquad (2)$$
$$\text{(Cont.)}$$

and the complete set of parity-equation residuals is

$$R_{12} = \frac{1}{\sqrt{2}} (\omega^B_{2y} - \omega^B_{1y} + \omega^B_{1z} - \omega^B_{2z})$$

$$R_{13} = \frac{1}{\sqrt{2}} (\omega^B_{1x} - \omega^B_{3x} + \omega^B_{3y} - \omega^B_{1y})$$

$$R_{14} = \frac{1}{\sqrt{2}} (\omega^B_{4x} - \omega^B_{1x} + \omega^B_{1z} - \omega^B_{4z})$$

$$R_{23} = \frac{1}{\sqrt{2}} (\omega^B_{2x} - \omega^B_{3x} + \omega^B_{2z} - \omega^B_{3z})$$

$$R_{24} = \frac{1}{\sqrt{2}} (\omega^B_{2x} - \omega^B_{4x} + \omega^B_{2y} - \omega^B_{4y})$$

$$R_{34} = \frac{1}{\sqrt{2}} (\omega^B_{3y} - \omega^B_{4y} + \omega^B_{3z} - \omega^B_{4z}) \qquad (3)$$

A similar set of equations holds for the accelerometers, with appropriate substitutions.

8.2   FDI Sensitivity

The orientation of the sensors with respect to the vehicle body axes and the resulting system of parity equations have a profound effect on the magnitude of sensor failures which can be detected and isolated. This aspect of the FDI problem for the redundant IMU sensor configuration and the EVT is explored in this section. SDOF instrument failures are assumed because it simplifies the discussion and gives insight into the area of FDI sensitivity, and because failure modes of this nature are a distinct possibility with TDOF gyros.

The parity equations attenuate the effect of a sensor failure, thus reducing its magnitude in the parity-equation residuals. The degree to which this occurs for the EVT algorithm is shown in Table 4, which gives the factor by which each of the sensor outputs is attenuated for all possible sensor configurations and failures. Thus, for example, the effect of a failure in instrument axis B1 will be attenuated by 0.258819 in parity equation R_{12}, -0.707107 in parity equation R_{13}, and 0.965926 in parity equation R_{14} for the four-instrument configuration. These are only three parity equations affected by the failure of this instrument axis. Table 4 was generated by substituting the equations for the components of the edge vectors into the parity equations. Uniform detectibility of the first failure exists with this algorithm since all of the coefficients of Table 4 obtained for it are permutations of each other.

The effect of the attenuation of the sensor outputs by the parity equations on the ability to detect and isolate failures is now considered. Consider the case with four instruments and an A1 axis failure with magnitude f. The effect on R_{12} will be 0.965926f, on R_{13} will be 0.707107f, and on R_{14} will be 0.258819f. Axis A1 will be declared failed if both $|R_{12}|$ and $|R_{13}|$ are greater than T. Therefore, the minimum value of failure detected will be f = T/0.707107 = 1.414214T.

The ability to detect failures degrades for the second and third failures; in certain instances, the magnitude of failure detected can be f = T/0.258819 = 3.863704T. This occurs when detection of a failure

Table 4. EVT algorithm FDI sensitivity; coefficients of parity equations.

Failed Sensors	Failed Axis	Parity-Equation Residual					
		R_{12}	R_{13}	R_{14}	R_{23}	R_{24}	R_{34}
−	A1	0.965926	0.707107	0.258819			
−	B1	0.258819	-0.707107	0.965926			
−	A2	-0.258819			0.965926	0.707107	
−	B2	-0.965926			0.258819	-0.707107	
−	A3		0.707107		-0.258819		0.965926
−	B3		-0.707107		-0.965926		0.258819
−	A4			-0.965926		0.707107	-0.258819
−	B4			-0.258819		-0.707107	-0.965926
1	A2				0.965926	0.707107	
1	B2				0.258819	-0.707107	
1	A3				-0.258819		0.965926
1	B3				-0.965926		0.258819
1	A4					0.707107	-0.258819
1	B4					-0.707107	-0.965926
2	A1		0.707107	0.258819			
2	B1		-0.707107	0.965926			
2	A3		0.707107				0.965926
2	B3		-0.707107				0.258819
2	A4			-0.965926			-0.258819
2	B4			-0.258819			-0.965926
3	A1	0.965926		0.258819			
3	B1	0.258819		0.965926			
3	A2	-0.258819				0.707107	
3	B2	-0.965926				-0.707107	
3	A4			-0.965926		0.707107	
3	B4			-0.258819		-0.707107	
4	A1	0.965926	0.707107				
4	B1	0.258819	-0.707107				
4	A2	-0.258819			0.965926		
4	B2	-0.965926			0.258819		
4	A3		0.707107		-0.258819		
4	B3		-0.707107		-0.965926		
1,2	A3						0.965926
1,2	B3						0.258819
1,2	A4						-0.258819
1,2	B4						-0.965926
1,3	A2					0.707107	
1,3	B2					-0.707107	
1,3	A4					0.707107	
1,3	B4					-0.707107	
1,4	A2				0.965926		
1,4	B2				0.258819		
1,4	A3				-0.258819		
1,4	B3				-0.965926		
2,3	A1			0.258819			
2,3	B1			0.965926			
2,3	A4			-0.965926			
2,3	B4			-0.258819			
2,4	A1		0.707107				
2,4	B1		-0.707107				
2,4	A3		0.707107				
2,4	B3		-0.707017				
3,4	A1	0.965926					
3,4	B1	0.258819					
3,4	A2	-0.258819					
3,4	B2	-0.965926					

in instrument axis B2 is attempted after sensor 1 has failed and has been removed from the cluster. Table 4 illustrates the degree to which all of the possible sensor configurations are affected by the attenuation of the sensor failures due to the parity equations.

Table 4 can also be used to provide qualitative information useful in distinguishing the wrong isolation of failures when the EVT is employed. This can be illustrated as follows. First, assume that a first failure is being detected and isolated. Then, assume that the A1 sensor axis fails with a magnitude just large enough so that the parity-equation residual $|R_{12}|$ exceeds the threshold. If the failure is large enough so that $|R_{13}|$ exceeds the threshold, the A1 axes will be declared to have failed and instrument 1 will be removed from the cluster. However, if $|R_{13}|$ does not exceed the threshold, the possibility for false isolation exists since the sensitivity coefficient associated with the parity-equation residual $|R_{23}|$ and a failure in axis A2 is 0.965926. In a high-noise environment with low failure-detection thresholds, it is possible for $|R_{23}|$ to exceed the threshold, and A2 will be selected as the failure axis rather than A1. Other sensor configurations that are prone to the wrong isolation of sensor failures can be determined from Table 4 in the same fashion.

8.3   FDI Thresholds

The generation of the thresholds for the TDOF gyros is considered first. An analytic expression for the output of the jth TDOF gyro is required to implement the approach defined in Section 7. This expression may be obtained from a consideration of Figures 6 and 7. The effects of quantization and rectangular integration are neglected and only first-order error terms are retained. The effects of the filtering required for the mid- and soft-failure channels are not considered at this point in the discussion. The resultant analytic expression for the output of the jth TDOF gyro is

$$m_{g_j} = \left(DT \cdot \frac{\pi}{180}\right)\left\{ H^G_{B_{j1}} \cdot p + H^G_{B_{j2}} \cdot q + H^G_{B_{j3}} \cdot r \right.$$

$$+ \lambda_{g_j} + \mu_{g_{j1}} \cdot p + \mu_{g_{j2}} \cdot q + \mu_{g_{j3}} \cdot r$$

$$+ \varepsilon_{g_j}\left(H^G_{B_{j1}} \cdot p + H^G_{B_{j2}} \cdot q + H^G_{B_{j3}} \cdot r \right)$$

$$+ \delta_{g_{j1}}\left(H^G_{B_{j1}} \cdot n_x + H^G_{B_{j2}} \cdot n_y + H^G_{B_{j3}} \cdot n_z \right)$$

$$+ \delta_{g_{j2}}\left(H^G_{B_{k1}} \cdot n_x + H^G_{B_{k2}} \cdot n_y + H^G_{B_{k3}} \cdot n_z \right)$$

$$+ \delta_{g_{j3}}\left(H^S_{B_{jk1}} \cdot n_x + H^S_{B_{jk2}} \cdot n_y + H^S_{B_{jk3}} \cdot n_z \right)$$

$$+ \delta_{g_{j4}}\left(H^G_{B_{j1}} \cdot n_x + H^G_{B_{j2}} \cdot n_y + H^G_{B_{j3}} \cdot n_z \right)^2$$

$$+ \delta_{g_{j6}}\left(H^S_{B_{jk1}} \cdot n_x + H^S_{B_{jk2}} \cdot n_y + H^S_{B_{jk3}} \cdot n_z \right)^2$$

$$+ \delta_{g_{j7}}\left(H^G_{B_{j1}} \cdot n_x + H^G_{B_{j2}} \cdot n_y + H^G_{B_{j3}} \cdot n_z \right)$$

$$\cdot \left(H^G_{B_{k1}} \cdot n_x + H^G_{B_{k2}} \cdot n_y + H^G_{B_{k3}} \cdot n_z \right)$$

$$+ \delta_{g_{j8}}\left(H^G_{B_{k1}} \cdot n_x + H^G_{B_{k2}} \cdot n_y + H^G_{B_{k3}} \cdot n_z \right)$$

$$\cdot \left(H^S_{B_{jk1}} \cdot n_x + H^S_{B_{jk2}} \cdot n_y + H^S_{B_{jk3}} \cdot n_z \right)$$

$$+ \delta_{g_{j9}} \left(H^G_{B_{j1}} \cdot n_x + H^G_{B_{j2}} \cdot n_y + H^G_{B_{j3}} \cdot n_z \right)$$

$$\cdot \left(H^S_{B_{jk1}} \cdot n_x + H^S_{B_{jk2}} \cdot n_y + H^S_{B_{jk3}} \cdot n_z \right)$$

$$+ \delta_{n_{18}} \left(H^G_{B_{k1}} \cdot p + H^G_{B_{k2}} \cdot q + H^G_{B_{k3}} \cdot r \right)$$

$$\cdot \left(H^S_{B_{jk1}} \cdot p + H^S_{B_{jk2}} \cdot q + H^S_{B_{jk3}} \cdot r \right)$$

$$+ \delta_{n_{19}} \left(H^G_{B_{j1}} \cdot p + H^G_{B_{j2}} \cdot q + H^G_{B_{j3}} \cdot r \right)$$

$$\left. \cdot \left(H^S_{B_{jk1}} \cdot p + H^S_{B_{jk2}} \cdot q + H^S_{B_{jk3}} \cdot r \right) \right\} \qquad \begin{array}{c} (4) \\ \text{(Cont.)} \end{array}$$

where

j = first input axis of instrument

= 1(A1), 3(A2), 5(A3), 7(A4)

k = second input axis of instrument

= 2(B1), 4(B2), 6(B3), 8(B4)

When Eq. (4) is substituted into the parity equations, the $H^G_{B_{j1}} \cdot p$, $H^G_{B_{j2}} \cdot p$, and $H^G_{B_{j3}} \cdot r$ terms disappear. The parity-equation residuals are then a function of the sensor error terms only. An analytic expression for the bound of the sensor errors is needed to generate dynamic thresholds for the parity-equation residuals. This expression may be obtained by assuming worst-case conditions: $\left| H^G_{B_{jk}} \right| = \left| H^S_{B_{jkl}} \right| = 1.0$; the signs of p, q, r and n_x, n_y, n_z and the elements of the geometry matrices are such that all terms add; a bound for the sums of these

terms is given by the sum of their absolute values; and the sensor errors are additive and bounded by their 3σ values. These assumptions lead to the following expression for an upper bound of the TDOF gyro errors

$$
\tilde{m}_{g_m} = \left(DT \cdot \frac{\pi}{180}\right) \left[\lambda_{g_m} + (\mu_{g_m} + \epsilon_{g_m})(|p| + |q| + |r|) \right.
$$

$$
+ \delta_{g_{\ell m}} (|n_x| + |n_y| + |n_z|)
$$

$$
+ \delta_{g_{nm}} (|n_x| + |n_y| + |n_z|)^2
$$

$$
\left. + \delta_{n_m} (|p| + |q| + |r|)^2 \right] \tag{5}
$$

By comparing this expression to Eq. (4), it is evident the $\delta_{g_{\ell m}}$ is an upper bound for $\delta_{g_{j1}} + \delta_{g_{j2}} + \delta_{g_{j3}}$, $\delta_{g_{nm}}$ is an upper bound for $\delta_{g_{j4}} + \delta_{g_{j6}} + \delta_{g_{j7}} + \delta_{g_{j8}} + \delta_{g_{j9}}$, and δ_{n_m} is an upper bound for $\delta_{n_{j8}} + \delta_{n_{j9}}$.

Equation (5) is now used to generate an analytic expression for the upper bound of the parity-equation residuals. This is done by noting that the maximum value of the body-axes components of the sensed angular rates, given by Eq. (2), is

$$
\omega_{g_m}^{B} = 2(0.577350)\tilde{m}_{g_m}
$$

Furthermore, the upper bound of the parity-equation residual is given by

$$
R_m = 0.707107(4.0\omega_{g_m}^{B})
$$

$$
= 3.266 \, \tilde{m}_{g_m}
$$

42

The final expression for the thresholds for the gyro parity equation for the hard-failure channel is

$$T_{g_h} = T_{g_{0h}} + 3.266 \; \tilde{m}_{g_m} \tag{6}$$

since only the sensor error terms remain. $T_{g_{0h}}$ is the constant portion of the threshold, which accounts for quantization, sensor noise, etc.

The absolute value of the parity-equation residual is compared to the output of Eq. (6) to ascertain whether a failure has occurred. Under normal operating conditions, with unfailed sensors present in the system, this threshold will not be exceeded. The dynamic portion of the failure-detection threshold is generated in real time using the last values of the angular rates and linear accelerations generated for the flight-control system.

Equation (6) is valid for the hard-failure channel in which no filtering of the signals is done. $T_{g_{0h}}$ is large relative to the dynamic portion of the threshold because of the significant effects of quantization. Modifications must be made to Eq. (6) for the detection of mid and soft failures. In order to make a valid comparison between the parity-equation residuals and the thresholds, it is necessary to filter each in an identical manner. When the effects of p, q, r and n_x, n_y, n_z on the sensor errors are linear, these signals can be filtered before the expression for the upper bound is derived. Thus, $|p_f| + |q_f| + |r_f|$ can be used in lieu of $|p| + |q| + |r|$ in Eq. (6). However, when the effects of these quantities are nonlinear, an expression for the upper bound of the nonlinear effect must be generated and then filtered. An example of this is with regard to the $(|n_x| + |n_y| + |n_z|)^2$ term. When filtering is present, this term is bounded by $[(|n_x| + |n_y| + |n_z|)^2]_f$ and not by $(|n_{xf}| + |n_{yf}| + |n_{zf}|)^2$.

43

The expression for the dynamic thresholds can be modified further to take advantage of the sensor configuration geometry to lower the minimum level of failure which can be detected. Consider the soft-failure channel. If the filtering is heavy enough so that the effects of quantization can be neglected, the constant for the soft-failure-detection threshold can be set equal to zero, so that the smallest possible failure can be detected. The level of soft failure which can be detected will then be governed by the dc value of the dynamic thresholds. The value is due in part to λ_{g_m}, but arises mainly from the effect of the normal acceleration level of $\approx$-1 g encountered during straight and level flight on the acceleration-dependent errors, i.e., the $\delta_{g_{\ell m}} |n_z|$ and $\delta_{g_{nm}} |n_z|^2$ terms of Eq. (5). For the sensor configuration under consideration, the terms of the input and spin sensor geometry matrices affecting n_z are 0.577350 ($H^G_{B_{j3}}$, $H^G_{B_{k3}}$, and $H^S_{B_{jk3}}$). Therefore, improved soft-failure-detection capability can be achieved by using $|0.577350n_z|$ in lieu of $|n_z|$ in the analytic expression for the threshold. This has the effect of lowering the dc value of the dynamic threshold and therefore the level of soft TDOF gyro failure which can be detected.

Incorporating into Eq. (5) and (6) the conclusions just drawn regarding the effect of filtering and sensor geometry on the thresholds leads to the following expression for the upper bound of the TDOF gyro errors and the failure-detection thresholds

$$
\tilde{m}_{g_{m_f}} = \left(DT \cdot \frac{\pi}{180} \right) \left\{ \lambda_{g_m} + (\mu_{g_m} + \varepsilon_{g_m})(|p_f| + |q_f| + |r_f|) \right.
$$

$$
+ \delta_{g_{\ell m}} (|n_{xf}| + |n_{yf}| + |0.577350n_{zf}|)
$$

$$
+ \delta_{g_{nm}} [(|n_x| + |n_y| + |0.577350n_z|)^2]_f
$$

$$
\left. + \delta_{n_m} [(|p| + |q| + |r|)^2]_f \right\} \tag{7}
$$

$$
T_g = T_{g_0} + 3.266\, \tilde{m}_{g_{m_f}} \tag{8}
$$

44

The minimum ideal level of gyro failure which can be detected with the EVT algorithm may be obtained from Eq. (7) and (8). Straight and level unaccelerated flight in nonturbulent air is assumed along with heavy filtering in the soft-failure-detection channel. These assumptions imply that $n_x = n_y = p = q = r = T_{g_0} = 0.0$ and $n_z = -1.0$ g. Using the 3σ values of the sensor errors leads to $T_{g_s} = 0.453$ degree per hour. As is shown in Section 8.5, this threshold can be decreased under penalty of an increased probability of the false detection of failures. The actual value of soft failure which can be detected depends upon the value of the failure-detection sensitivity coefficient presented in Table 4. The smallest failure detected will be $0.453/0.707107 = 0.640$ degree per hour.

A similar development has been carried out to determine an expression for the accelerometer FDI system thresholds. The jth accelerometer output is obtained from Figure 5 and is given by

$$
\begin{aligned}
m_{a_j} = (DT \cdot G\phi)\Bigg\{ & H^A_{B_{j1}} \cdot n_x + H^A_{B_{j2}} \cdot n_y + H^A_{B_{j3}} \cdot n_z \\
& + \lambda_{a_j} + \mu_{a_{j1}} \cdot n_x + \mu_{a_{j2}} \cdot n_y + \mu_{a_{j3}} \cdot n_z \\
& + \varepsilon_{a_j}\left(H^A_{B_{j1}} \cdot n_x + H^A_{B_{j2}} \cdot n_y + H^A_{B_{j3}} \cdot n_z \right) \\
& + \alpha_{IP_j}\left(H^A_{B_{j1}} \cdot n_x + H^A_{B_{j2}} \cdot n_y + H^A_{B_{j3}} \cdot n_z \right) \\
& \cdot \left(H^P_{B_{j1}} \cdot n_x \cdot H^P_{B_{j2}} \cdot n_y + H^P_{B_{j3}} \cdot n_z \right) \\
& + \beta_{II_j}\left(H^A_{B_{j1}} \cdot n_x + H^A_{B_{j2}} \cdot n_y + H^A_{B_{j3}} \cdot n_z \right)^2 \Bigg\}
\end{aligned}
$$

where

$$j = 1, 2, \ldots, 8 = A1, B1, \ldots, B4$$

45

Performing the same simplifications and steps as in the case of the gyros leads to the following expression for the upper bound of the accelerometer error

$$\tilde{m}_{a_{m_f}} = (DT \cdot G\phi) \left\{ \lambda_{a_m} + \left(\mu_{a_m} + \varepsilon_{a_m} \right)\left(\left| n_{xf} \right| + \left| n_{yf} \right| + \left| 0.577350 n_{zf} \right| \right) \right.$$

$$\left. + \left(\beta_{II_m} + \alpha_{IP_m} \right)\left[\left(\left| n_x \right| + \left| n_y \right| + \left| 0.577350 n_z \right| \right)^2 \right]_f \right\}$$

Strictly speaking, since $\mu_{a_{j3}}$ in the equation for m_{a_j} is not multiplied by $H^A_{B_{j3}}$, the misalignment error coefficient used to obtain μ_{a_m} must be divided by 0.577350. This was not done during this study.

The final expression for the accelerometer threshold is then given by

$$T_a = T_{a_0} + 3.266 \tilde{m}_{a_{m_f}}$$

The minimum level of accelerometer threshold attainable for the EVT algorithm is 1350 micro-g for straight and level unaccelerated flight in nonturbulent air. The smallest actual accelerometer failure which can be detected because of the failure-detection sensitivity of the algorithm is 1350 micro-g/0.707107 = 1909 micro-g. This value may be adjusted downward under the penalty of an increased probability of false alarm as is discussed in Section 8.5.

One additional important conclusion can be drawn regarding the thresholds determined for the EVT. The thresholds are not a function of the number of instruments in the configuration. This means that the lower failure-detection sensitivity evident in Table 4 for a configuration with fewer sensors in the cluster is not compensated for by a corresponding lowering of the failure-detection thresholds.

8.4 Simulation Results

This section presents and discusses the results obtained with the simulation described in Section 3 for the EVT algorithm. Presented are time histories of the parity-equation residuals and failure-detection thresholds obtained using the equations and techniques presented previously. Time histories were obtained for two vehicle trajectories: the maneuvering trajectory, which is presented in Figure 8, and straight and level unaccelerated flight, which was taken to gain a better understanding of the FDI capability of the EVT without the effects of maneuvers.

Figure 12 shows the value of one of the parity-equation residuals obtained. The top half of the figure shows the residual R_{24} unfiltered, lagged with the filter used for the midvalue-failure channel, and passed through the second-order filter used for the soft-failure channel. The unfiltered parity-equation residual is random in nature due to the effect of the sensor quantization. Its peak value is in the vicinity of 258 degrees per hour. Filtering reduces the magnitude of the parity-equation residuals as evidenced by these variables for the mid- and soft-failure channels. The magnitude of these signals is indicative of the level of sensor failure which can be detected in each of these channels.

The corresponding parity-equation residuals obtained for the maneuvering-flight trajectory are also shown in Figure 12. The unfiltered residual corresponds very closely in character and magnitude to that obtained for the maneuvering trajectory. The vehicle maneuvers have no apparent effect on this parameter. The effect of the maneuvers on the lagged midchannel parity-equation residual is also minor at most. A slight increase in magnitude at some point in the trajectory occurred as evidenced by the change in scale from that obtained for the non-maneuvering trajectory. This point, however, does not occur in Figure 12, since only the data points at 1-second intervals are plotted, although each calculated point is used to set the scale.

The effect of the vehicle maneuvers is very evident in the soft-failure-channel parity-equation residual. The magnitude of the signal obtained with the maneuvering trajectory is on the order of four times

47

STRAIGHT, LEVEL FLIGHT
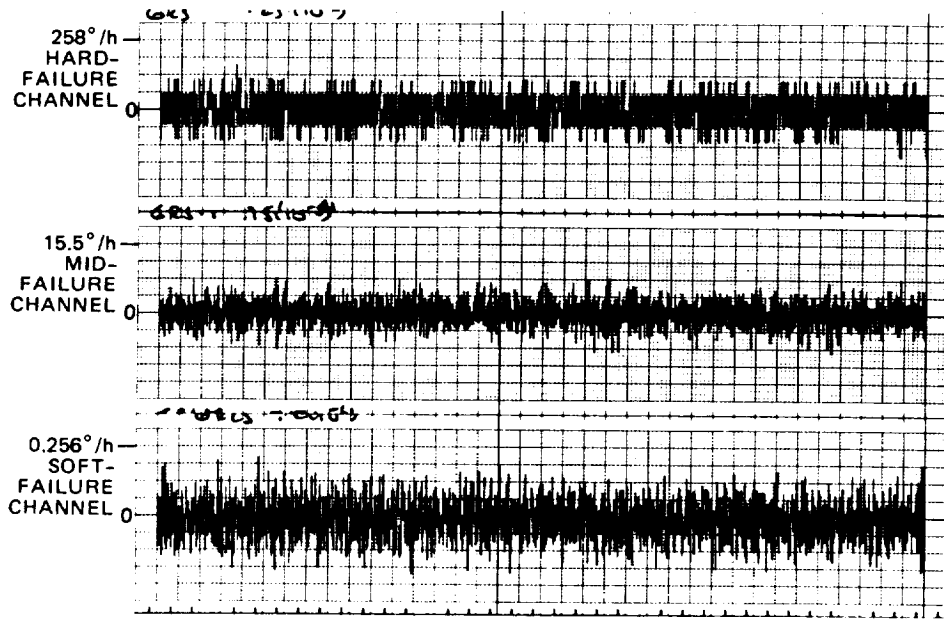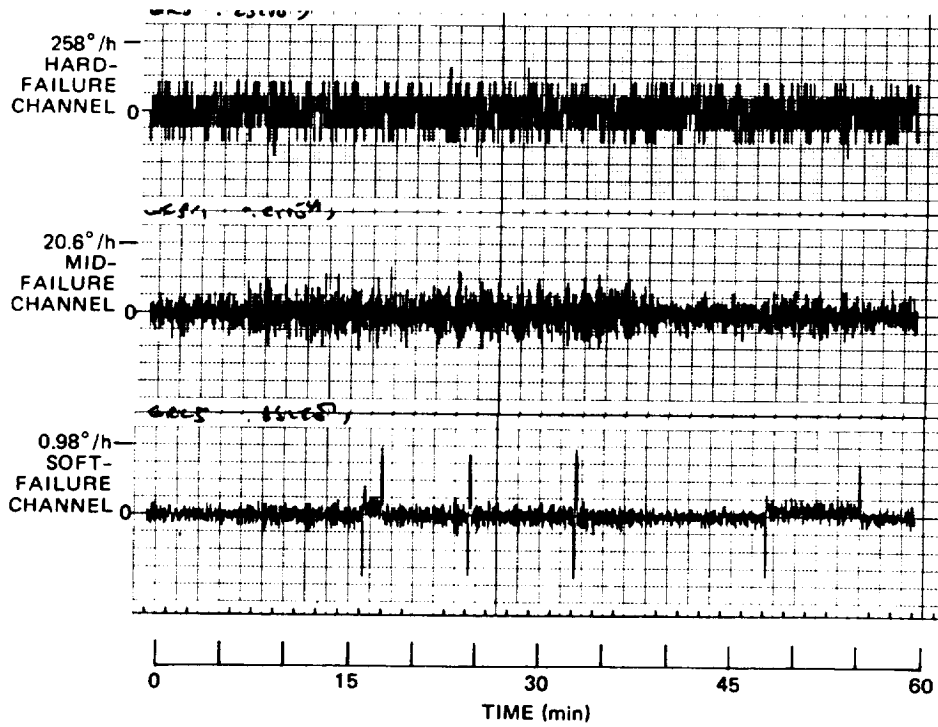

DYNAMIC TRAJECTORY

Figure 12.   TDOF gyro parity-equation residuals:
EVT, no sensor failure.

that obtained for straight and level flight. This dictates the need for dynamic failure-detection thresholds. If a constant threshold were used, it would have to be large enough to account for the effect of all of the possible maneuvers that the vehicle would undergo. This, however, would compromise the failure-detection capability of the system during straight and level flight since the thresholds would be much larger than required. A much more appealing solution is to adopt the approach advocated in this report of having thresholds which are constant during straight and level flight but which also include the terms affected by the dynamics of the vehicle so as to account for these effects.

Typical hard, mid, and soft accelerometer FDI system parity-equation residuals are presented in Figure 13 for both the straight and level and maneuvering trajectories. The residual R_{23} is the particular one shown. The hard-failure-channel residual is random in nature and of the same magnitude for both trajectories. This randomness is of course due to quantization. The magnitude of this residual is also quite small, indicating that the level of hard failure which can be detected will also be quite small.

The soft-failure-channel residuals are constant for nonmaneuvering flight. The maneuvers have very little effect on these variables. The constant portion arises because of the effect of the 1-g steady-state normal acceleration on the sensor errors. This implies that constant thresholds may be suitable for the soft-failure-detection channel and for the whole accelerometer FDI system.

The mid-failure-channel parity-equation residuals are just less heavily filtered versions of the soft-failure-channel parity-equation residuals. They have a slightly larger magnitude because of the higher noise level. Since the magnitude of the hard-failure-channel parity-equation residuals is so small and the soft-failure-channel residuals are so much cleaner, the need for a mid-failure channel is not apparent for the accelerometers.

The threshold levels obtained for the EVT algorithm with the technique outlined in Section 8.3 are now presented and discussed.

49

STRAIGHT, LEVEL FLIGHT

3885 µg —
HARD-
FAILURE
CHANNEL 0

233 µg —
MID-
FAILURE
CHANNEL 0

132 µg —
SOFT-
FAILURE
CHANNEL 0

DYNAMIC TRAJECTORY

3885 µg —
HARD-
FAILURE
CHANNEL 0

233 µg —
MID-
FAILURE
CHANNEL 0

140 µg —
SOFT-
FAILURE
CHANNEL 0

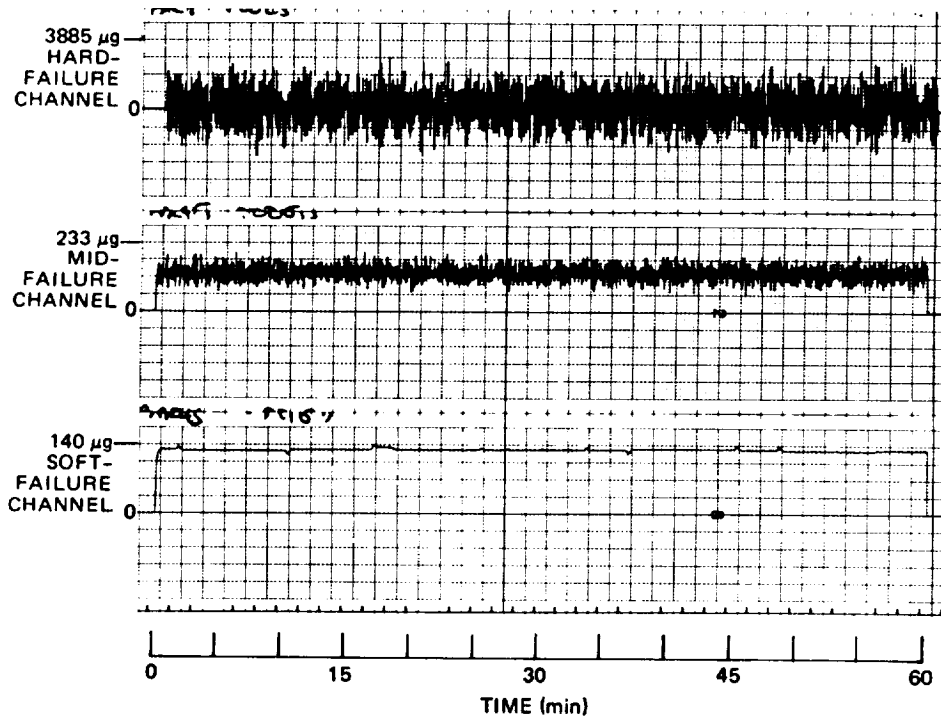0   15   30   45   60
TIME (min)
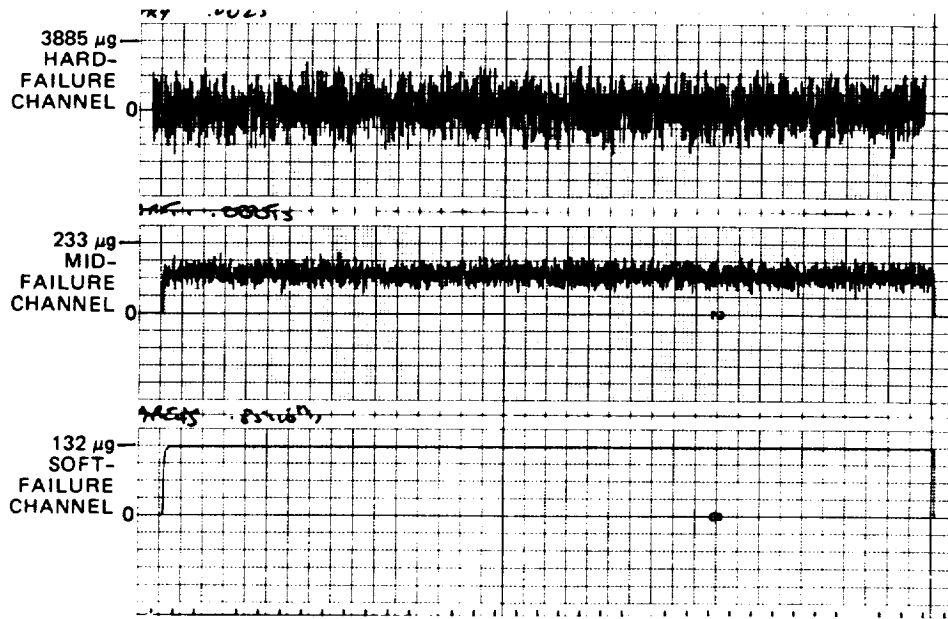
Figure 13.   Accelerometer parity-equation residuals:
EVT, no sensor failure.

50

The first item that must be addressed is the selection of the constant portion of the thresholds included to account for quantization, etc. Based upon the data presented in Figures 12 and 13, as well as those data obtained for other simulation runs, the constant thresholds given in Table 5 were selected. The constant portion of the thresholds for the soft-failure channels was set at zero so that the smallest possible failures could be detected.

Table 5. Constant thresholds for the EVT algorithm.

Instrument	Channel	Threshold
Gyro	Hard	227°/h
	Mid	20.63°/h
	Soft	0.0°/h
Accelerometer	Hard	6019 µg
	Soft	0.0 µg

The EVT gyro thresholds are presented in Figure 14 for both maneuvering and nonmaneuvering flight. The hard-failure- and mid-failure-channel thresholds are basically the same for both trajectories, with the level dictated by the constant portion of the threshold. The effects of the maneuvers are not really evident, except for the soft-failure channel where the threshold is an order of magnitude larger for the maneuvering trajectory than for straight and level flight. The soft-failure-detection threshold for level flight is in the vicinity of 0.7 degree per hour. This value defines the level of FDI capability which can be expected with the EVT, and it is slightly larger than the ideal value mentioned in Section 8.3. One of the reasons for this discrepancy is the effect of a nonzero steady-state value of n_x. This was neglected in arriving at the ideal value and accounts for a 10-percent difference. Furthermore, the vehicle is continually excited by turbulence during the trajectory, which increases the level of the threshold. During flight in nonturbulent air, the level of the soft-failure-detection threshold

51

STRAIGHT, LEVEL FLIGHT
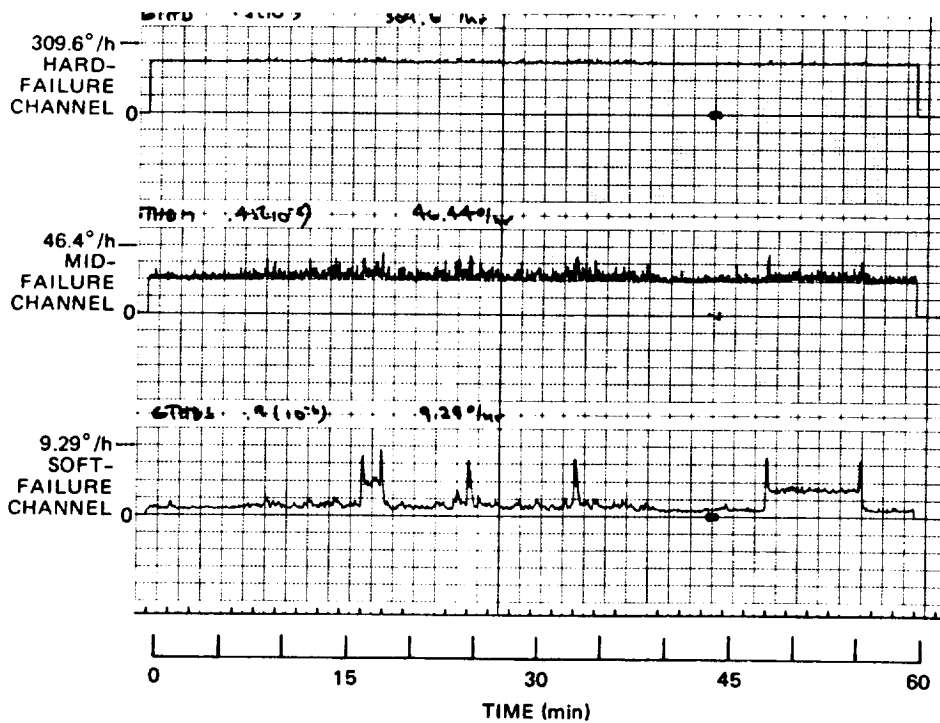

DYNAMIC TRAJECTORY

TIME (min)
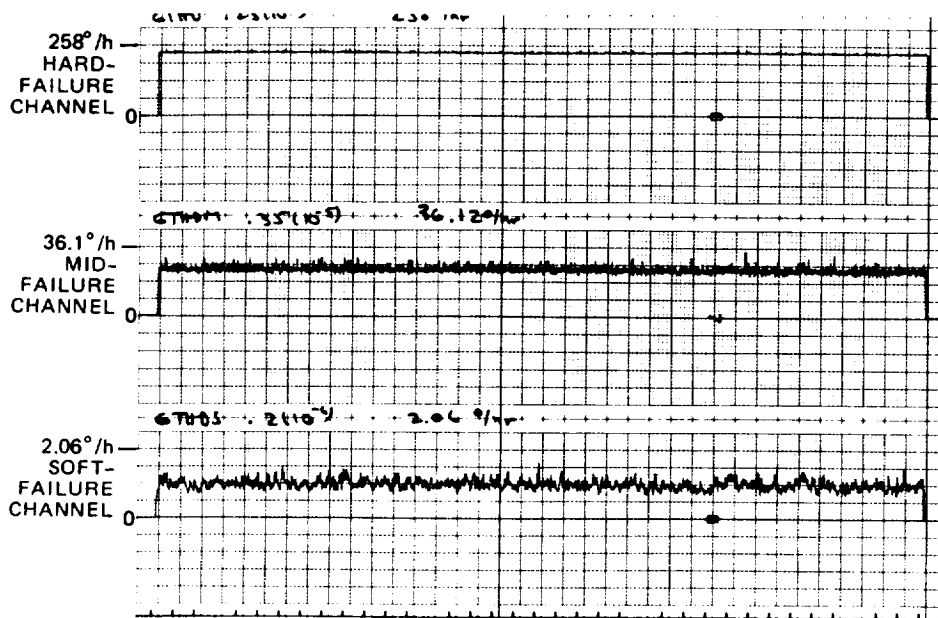
Figure 14. TDOF gyro failure-detection thresholds: EVT.

closely approximates the ideal value. The fact that the minimum level of the soft-failure-detection threshold is less than the maximum value of the soft-failure-channel parity-equation residual shown in Figure 12 dictates the need for dynamic thresholds.

The accelerometer thresholds are presented in Figure 15. These thresholds reflect the conclusions drawn previously concerning the accelerometer parity-equation residuals. No mid-failure-channel threshold is shown. The maneuvers have only a slight impact on the soft-failure-detection threshold. The level of the hard-failure-detection threshold is quite low, dictated by the sum of the constant value of the thresholds given in Table 5 and the soft-failure-detection threshold shown in Figure 15.

8.5   Probability of False Alarm

In this section, a simplified analysis is carried out to arrive at an upper bound for the probability of the false detection of the first soft sensor failure using the EVT algorithm. This reflects an effort to determine the degree to which the nominal value of the soft-failure-detection theshold can be lowered to achieve better navigation-system performance without significantly degrading the system because of false alarms. Assume that the vehicle is flying straight and level in a low-turbulence environment. A simplified expression for the gyro sensor error, obtained from Eq. (4), which is valid under these assumptions is

$$
\tilde{m}_{g_j} = \left(DT \cdot \frac{\pi}{180} \right) \left[\lambda_{g_j} - (0.577350) \delta_{g_{j1}} \right.
$$

$$
\left. + (0.577350)^2 \left(\delta_{g_{j4}} + \delta_{g_{j6}} + \delta_{g_{j7}} + \delta_{g_{j8}} + \delta_{g_{j9}} \right) + \eta \right]
$$

where η is assumed to be zero-mean Gaussian noise with standard deviation σ_η. The sensor errors are assumed to be Gaussian distributed variables
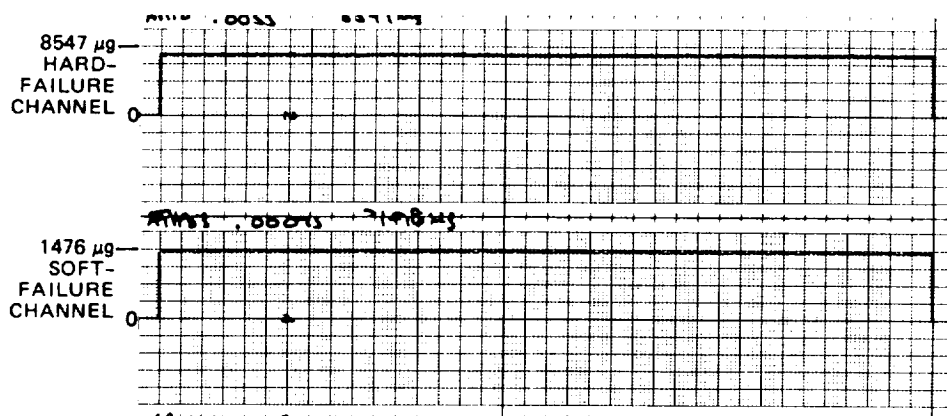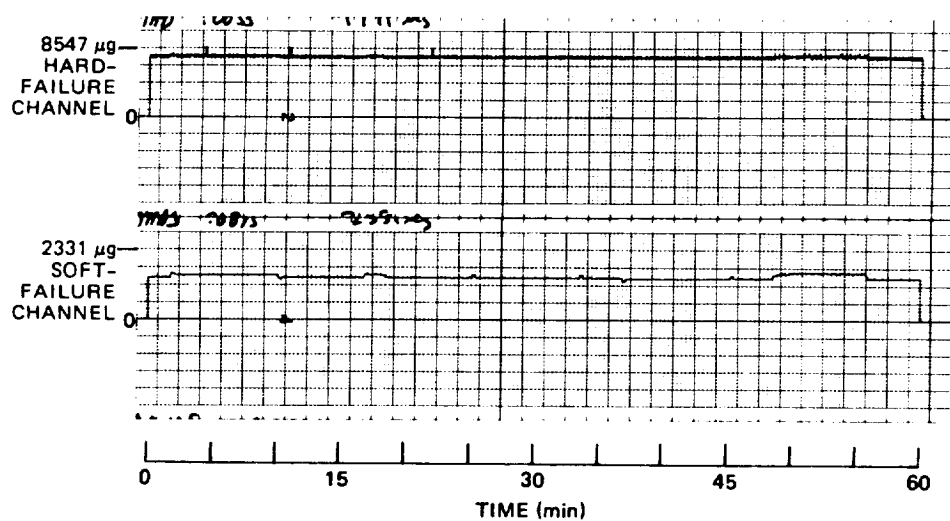
Figure 15.   Accelerometer failure-detection thresholds: EVT.

54

with 1σ values equal to the nominal values given in Table 1. This leads to the following result

$$\sigma_{\tilde{m}_{g_j}}^2 = \left(DT \cdot \frac{\pi}{180}\right)^2 (0.000330555 + \sigma_\eta^2)$$

since the variance of the total is equal to the sum of the variances. A continued analysis leads to the result that the variance of the errors of the body-axes components of the sensed angular rates is

$$\sigma_{\tilde{\omega}}^2 = 0.666666\sigma_{\tilde{m}_{g_j}}^2$$

and that the variance of the parity-equation residuals is

$$\sigma_{R_g}^2 = 2.0 \; \sigma_{\tilde{\omega}}^2$$

$$= 1.33333 \left(DT \cdot \frac{\pi}{180}\right)^2 (0.000330555 + \sigma_\eta^2)$$

The declaration of a false failure requires that two parity-equation residuals exceed the threshold simultaneously. There are 12 ways in which this can occur, as is evident from the FDI equations given in Section 8. Since the parity-equation residuals are each Gaussian random variables, the probability of two of them exceeding a threshold simultaneously is governed by a joint Gaussian probability density function. Furthermore, the joint density function is highly correlated since noise in one sensor output can affect two parity-equation residuals simultaneously.

Rather than tackling the approach just described, which is very complicated, a simplified approach to the problem was pursued and an upper bound for the probability of false alarm determined. In

55

doing this, it must be realized that the probability of one parity-equation residual exceeding the threshold is greater than the probability of that residual and any other residual exceeding the threshold. That is, $P(|R_{jk}| > T) \geq P(|R_{ij}| > T$ and $|R_{k\ell}| > T)$. Since there are 12 ways for a false alarm to occur, and the probability of a parity-equation residual is the same for each residual, the probability of the false detection of the first sensor failure is given by

$$P_{FA} \leq 12P(|R_{ij}| \geq T)$$

The probability of exceeding a given threshold level is obtained from a table of Gaussian probability distribution function values. The two-sided value must be used since the threshold can be exceeded both positively and negatively.

Figure 16 shows the values of the thresholds obtained as a function of the sensor noise level and the ratio of the threshold level to the standard deviation of the parity-equation-residual noise. Also presented in this figure is the upper bound for the probability of false alarm as a function of the ratio T_g/σ_{R_g}. The value of the nominal soft-failure-detection threshold was given in Section 8.3 as 0.453 degree per hour. This value is also indicated in Figure 16 so that its probability of false alarm can be evaluated.

A similar analysis has been carried out for the accelerometers. The results are presented in Figure 17.
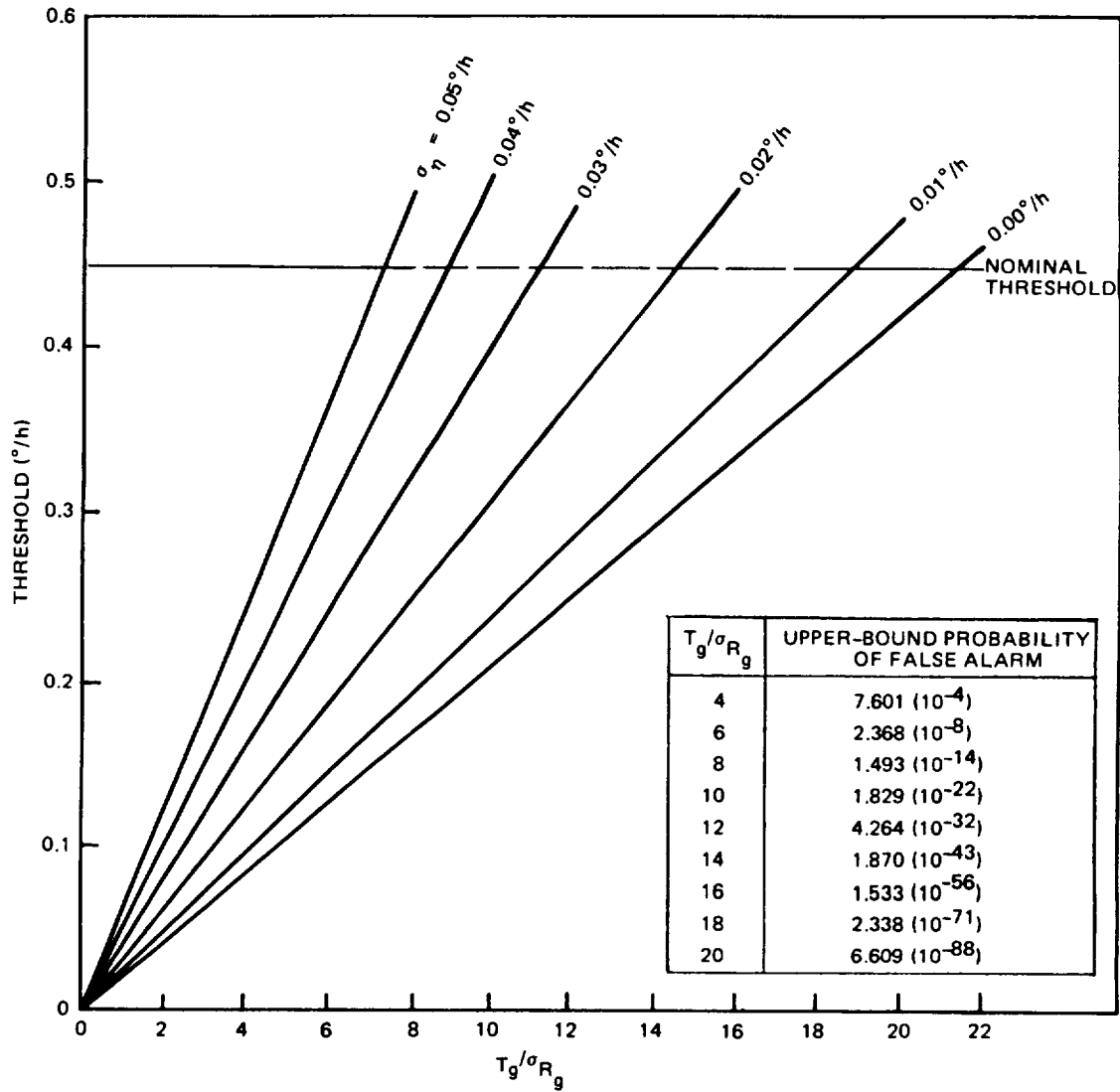
56

Figure 16. Gyro soft-failure-detection thresholds vs. sensor noise
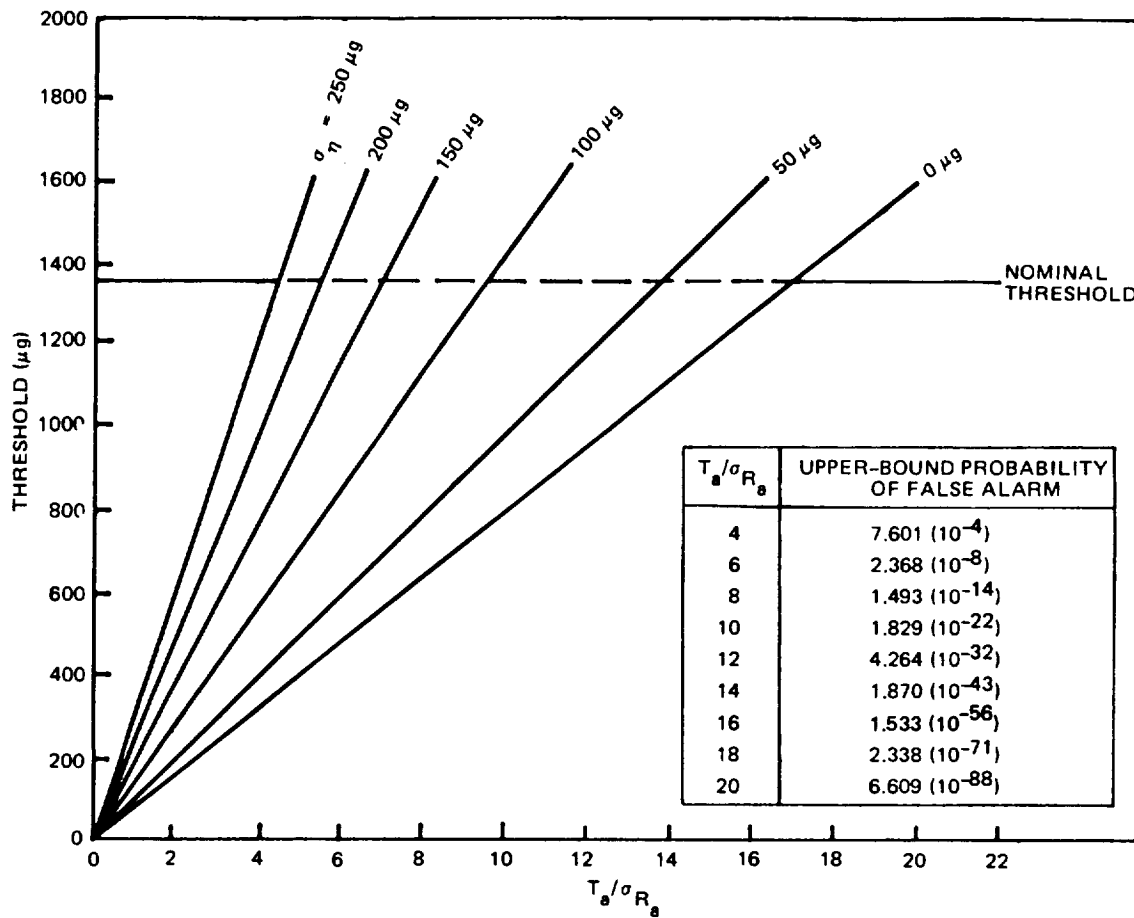level and ratio of threshold to nominal parity-equation-
residual noise level.

57

T_a/σ_{R_a}	UPPER-BOUND PROBABILITY OF FALSE ALARM
4	7.601 (10^{-4})
6	2.368 (10^{-8})
8	1.493 (10^{-14})
10	1.829 (10^{-22})
12	4.264 (10^{-32})
14	1.870 (10^{-43})
16	1.533 (10^{-56})
18	2.338 (10^{-71})
20	6.609 (10^{-88})

Figure 17. Accelerometer soft-failure-detection thresholds vs. sensor noise level and ratio of threshold to nominal parity-equation-residual noise level.

SECTION 9

THE GENERALIZED LIKELIHOOD TEST (GLT)

9.1   Description

The GLT algorithm is briefly described in this section. Consider first the hard-failure channel. In the absence of sensor failures, the measurement equation is

$$\hat{m} = \hat{H}\hat{\omega} + \hat{\eta} \tag{9}$$

A set of parity equations is defined by

$$\hat{\rho} = \hat{V}\hat{m} \tag{10}$$

where

$$\hat{V}\hat{H} = 0$$

$\hat{V}$ is assumed to be of dimension $(n - 3) \times n$. The matrix $\hat{V}$ can be chosen so that

$$\hat{V}\hat{V}^T = I$$

Substituting Eq. (9) into Eq. (10) yields

$$\hat{\rho}_N = \hat{V}\hat{\eta}$$

In the absence of sensor failures, $\hat{\rho}_N$ depends only on the measurement noise. If sensor j experiences a bias-type failure of magnitude f, and that failure is manifest as an apparent bias shift of magnitude b in measurement j, then

$$\hat{\rho}_F = \hat{V}\hat{\eta} + \hat{v}_j b$$

The difference in the statistics of $\hat{\rho}_N$ (in the absence of failures) and $\hat{\rho}_F$ (in the presence of failures) provides a basis for detecting and iso-lating failures. The problems of detecting and isolating sensor failures fall within the general framework of composite hypothesis tests, since the sign as well as the magnitude of the bias failure is unknown a priori.

A GLT formation of the detection and isolation problems has been developed. Assume single-axis failures initially. The GLT decision functions for detection and isolation are

$$DF_D = \hat{\rho}^T\hat{\rho} \tag{11}$$

$$DF_{I_j} = \frac{\left(\hat{\rho}^T\hat{v}_j\right)^2}{\hat{v}_j^T\hat{v}_j}, \quad j = 1,2,\ldots,n \tag{12}$$

These decision functions are strictly functions of the parity-equation residuals, $\hat{\rho}$. The detection decision is made by comparing DF_D (which is the sum of the squares of the parity-equation residuals) to a detection threshold. A sensor failure results in a change in the mean value of a sensor output, the parity-equation residuals, and the failure-detection function. The isolation decision is then made by determining $\max_j (DF_{I_j})$. The value of j that maximizes DF_{I_j} identifies the sensor that is most likely to have failed.

The preceding discussion assumes a set of n SDOF instruments.
The extension to TDOF sensors requires certain modifications to reflect
the characteristics of these instruments.[6] Correlation between the
noise present in the two measurements derived from a TDOF sensor is
possible. One approach is to assume no correlation, design the FDI
algorithms accordingly, and examine the degradation of FDI performance
which occurs due to the presence of the nonzero values of correlation.
This approach leads to the simplest algorithms and is preferred when
the performance penalty incurred for nonzero values of correlation is
acceptably small. In this case, the detection problem formulation is
not changed, and the appropriate decision function is given by Eq. (11).

In formulating the isolation problem, another characteristic of
TDOF sensors must be considered. A TDOF sensor failure may be reflected
in either or both of its measurement axes. In practice, a failure ob-
served in either axis is sufficient to disqualify the data from both of
the sensor axes. Thus, isolation of a failed sensor rather than of a
failed axis is sufficient. The isolation problem then involves testing
only n/2 hypotheses. The GLT decision function for isolation which
corresponds to Eq. (12) is

$$DF_{I_j} = \hat{\rho}^T \, \hat{V}_j (\hat{V}_j^T \hat{V}_j)^{-1} \, \hat{V}_j^T \hat{\rho} \qquad j = 1, 2, \ldots, n/2 \qquad (13)$$

where $\hat{V}_j = [\hat{v}_{2j-1}, \hat{v}_{2j}]$ and $\hat{v}_{2j-1}$, $\hat{v}_{2j}$ are the two columns of the $\hat{V}$
matrix associated with TDOF sensor j.

The detection and isolation of the mid and soft failures is ac-
complished using the same decision functions as for the hard-failure
channel. The only exception is that the appropriately filtered parity-
equation residuals are used in lieu of the unfiltered ones.

The determination of the performance probabilities for the GLT
algorithm such as the probability of false alarm, missed detection, etc.,
is a complex analytic task. For this reason, it was not carried out

under this study for the sensor configuration of interest. A qualitative approach was employed instead as discussed in Section 9.2. The analytic technique for generating these probabilities is demonstrated in References 6 and 7 for sensor configurations other than the one discussed here.

9.2 Parity Equations

The GLT algorithm requires sets of parity equations with the properties defined in Section 9.1. The parity-equation sets are obtained via an algorithm specified in Reference 11 using a least-squares approach. One set of equations is needed for each possible potential sensor configuration because of the reconfiguration of the sensor cluster following instrument failures. Tables 6 and 7 provide information concerning the number of sensors, number of parity-equation sets needed, and equations within each set. The sensor configurations to which these sets

Table 6. GLT parity-equation information.

Number of Instruments	Instruments	Number of Parity Equations
4	1,2,3,4	5
3	1,2,3	3
	2,3,4	
	3,4,1	
	4,1,2	
2	1,2	1
	2,3	
	3,4	
	4,1	
2	1,3	1
	2,4	

Table 7. Parity-equation matrices for GLT algorithm.

0.79056	0.0	-0.15811	-0.43197	0.15811	-0.31623	-0.15811	0.11575	Four Instruments
0.0	0.79056	0.11575	-0.15811	-0.31623	0.15811	-0.43197	-0.15811	
0.0	0.0	0.76590	-0.06528	-0.08277	-0.53507	0.19585	-0.27862	Three Instruments
0.0	0.0	0.0	0.63964	0.16322	-0.42451	-0.58442	0.20607	
0.0	0.0	0.0	0.0	0.68301	0.18301	-0.18301	-0.68301	Two Instruments Adjacent

Two Instruments-Separated

| 0.5 | -0.5 | 0.5 | -0.5 |

of parity equations apply is also given. Thus, four systems of parity equations are needed to detect the first two failures. A single system of parity equations is applicable to the four-instrument cluster. A single system of parity equations is applicable to all possible sets of three-instrument groups since they are rotations of each other. Two systems of parity equations are needed for the two-instrument-sensor clusters: one when the two instruments are adjacent to each other and the other when the instruments are opposite each other.

Several assumptions have been made in the following discussion for purposes of convenience. When the three-instrument configuration is considered, it is assumed that the unfailed instruments are 1, 2, and 3 and that instrument 4 has failed. Similarly, the pairs 1,2 and 1,3 are used for the two-instrument configurations. All of the other possible two- and three-instrument configurations are rotations or permutations of these and involve just a renumbering of the sensors. Assumptions are also made with regard to the particular axis within a configuration which fails. The results are applicable to other axes as well because of the reordering which can be done.

The systems of parity equations applicable to the redundant IMU considered in this study are presented in Table 7. The set of parity equations for the three-instrument configurations and the parity equation for the two-adjacent-instrument configurations are subsets of the

five parity equations for the four-instrument IMU. The parity equation
for the case where the two instruments are opposite each other is also
presented in Table 7. Because of the symmetry of this configuration,
the equation is the sum and difference of the instrument measurements
multiplied by a constant.

The failure-decision function associated with the GLT algorithm
is the sum of the squares of the parity-equation residuals (see Eq. (11)).
A measure of the ability of this algorithm to detect failures is given
by the square root of the sum of the squares of the coefficients of the
columns of the parity-equation matrix. The failure-decision function
is the square of the just-mentioned number times the magnitude of the
failures squared (for perfect instruments). Thus, the smaller the value
of this number, the greater the magnitude of a detectable failure re-
quired for a given value of failure-detection threshold.

The values of the failure-detection sensitivity coefficients or
square root of the sum of the squares of the elements of a column of
the parity-equation matrix are presented in Table 8 for the redundant
IMU. From the information contained in this table, it is evident that
the first failure is uniformly detectable because of the symmetry of

Table 8. GLT failure-detection sensitivity.

Number of Instruments	Failed Axis							
	A1	B1	A2	B2	A3	B3	A4	B4
4	0.7906	0.7906	0.7906	0.7906	0.7906	0.7906	0.7906	0.7906
3	0.7659	0.6430	0.7071	0.7071	0.6430	0.7659	–	–
2 (adjacent)	0.6830	0.1830	0.1830	0.6830	–	–	–	–
2 (separated)	0.5	0.5	–	–	0.5	0.5	–	–

the instrument cluster. The columns of the $\hat{V}$ matrix satisfy the uniform detectability constraint

$$\hat{v}_j^T \hat{v}_j = \frac{n-3}{n} \quad j = 1,2,\ldots,n$$

The failures associated with the three-instrument clusters are also fairly uniformly detectable, although the magnitude of failure which can go undetected is larger for three instruments than it is for four. When failure detection for the two-instrument clusters is considered, it is once again evident that a failure larger than that needed in the three- or four-instrument cases has to occur before it is detected. In the majority of cases, the magnitude of failure which will be detected is approximately the same. The only case where a disparity exists is when it is necessary to detect a failure in the two inner axes when two adjacent sensors remain. In this instance, the failure must be 4.3202 times larger than the failure magnitude detected for the first failure.

The GLT failure-isolation decision function is given by Eq. (12) for single-axis failures and by Eq. (13) for TDOF failures. The failed sensor is chosen to be the one corresponding to the largest failure-isolation coefficient. The incorrect isolation of a sensor failure arises from the presence of sensor noise, which could cause the isolation coefficient corresponding to a sensor axis other than the failed one to be largest.

The GLT algorithm failure-isolation sensitivity may be examined by comparing the normalized magnitudes of the failure-isolation coefficients for different failed-instrument axes. A measure of the ability of the GLT algorithm to isolate failures correctly and not to select the wrong sensor as having failed is given by the ratio of the largest isolation coefficients for a given failure.

The values of the failure-isolation coefficients obtained for the redundant IMU configuration with the GLT algorithm are presented in Table 9 for the four-instrument and three-instrument sensor configurations. It is only possible to detect (not isolate) a failure with two instruments, so the two-instrument case was not considered; single-axis failures are assumed. A similar exercise could be carried out for dual-axis failures via Eq. (13), but this has not been done so that a comparison could be drawn with the corresponding material in Section 9.

Table 9. GLT failure-isolation coefficients for single-axis failure.

Coefficient of Isolation Function	Failed Axis						
	Four Instruments	Three Instruments					
	A1	A1	B1	A2	B2	A3	B3
A1	0.625	0.587	0.004	0.007	0.286	0.038	0.007
B1	0.0	0.006	0.413	0.029	0.135	0.362	0.054
A2	0.025	0.008	0.0241	0.500	0.020	0.112	0.336
B2	0.1866	0.336	0.112	0.020	0.500	0.0241	0.008
A3	0.025	0.054	0.362	0.135	0.029	0.413	0.006
B3	0.100	0.077	0.038	0.286	0.007	0.004	0.587
A4	0.025	-	-	-	-	-	-
B4	0.013	-	-	-	-	-	-

The ability to correctly isolate the first axis failure for the four-instrument configuration should be quite good since the ratio of the second largest isolation coefficient to the largest is 0.2986. However, the ability to correctly isolate failures is degraded for the three-sensor configuration. For example, difficulties may arise, incorrectly isolating axis B1 as having failed since the ratio of the

isolation coefficient for axis A3 to that of axis B1 is 0.8765. Axis A3 may be falsely chosen as the failed instrument axis in a noisy environment. Other potential difficulties in isolation which may arise are between axes A1 and B2 when axis A1 has failed and between axis A2 and B3 when axis A2 has failed. The same difficulty also arises if the other sensor fails in the previous cases.

9.3   FDI Thresholds

The thresholds used with the GLT algorithm are generated using a method very similar to that used for the EVT algorithm. They also consist of a constant portion and a dynamic portion. The dynamic thresholds are again generated from an analytic expression for the upper bound of the sensor errors and parity-equation residuals. However, the failure-decision function is different for the two algorithms and this is reflected in the generation of the dynamic thresholds. For the EVT algorithm, the parity-equation residuals are compared directly to the thresholds for failure detection. With the GLT algorithm, the failure-decision function is the sum of the squares of the parity-equation residuals.

Consider the development of the thresholds for the TDOF gyros. Equation (7) is still valid for the upper bound of the TDOF gyro errors. The parity-equation residuals are given by

$$\rho_{g_i} = \sum_{j=1}^{n} V_{ij} \, m_{g_j} \qquad i = 1,2,\ldots,n-3$$

The residuals are a function of the sensor errors only because of the manner in which the $\hat{V}$ matrix was selected.

An upper bound for ρ_{g_i} is

$$\rho_{g_m} = \tilde{m}_{g_{mf}} \left[\sum_{j=1}^{n} |v_{ij}| \right]_m$$

The failure-decision function is

$$DF_{D_g} = \sum_{i=1}^{n-3} \rho_{g_i}^2$$

Therefore, an upper bound for DF_{D_g} is given by

$$T_g = (n - 3) \rho_{g_m}^2$$

$$= (n - 3) \left\{ \tilde{m}_{g_{mf}} \left[\sum_{j=1}^{n} |v_{ij}| \right]_m \right\}^2$$

$$(14)$$

The constant portion of the threshold is added to this when it is necessary to account for quantization and sensor noise as in the hard-failure channel.

A similar expression results for the accelerometer thresholds, except that $\tilde{m}_{a_{mf}}$ is used instead of $\tilde{m}_{g_{mf}}$.

One significant conclusion which can be drawn regarding the GLT thresholds is that they are a function of the number of parity equations. Thus, when fewer sensors are present, fewer parity equations are required, and the thresholds can be lowered to compensate for the lower failure-detection sensitivity which occurs when this happens.

68

The minimum level of failure which can be detected with the GLT algorithm can be determined from Eq. (14) to provide a comparison with the value obtained for the EVT algorithm. Under the assumptions of straight and level flight, etc., the nominal thresholds obtained for the GLT algorithm are
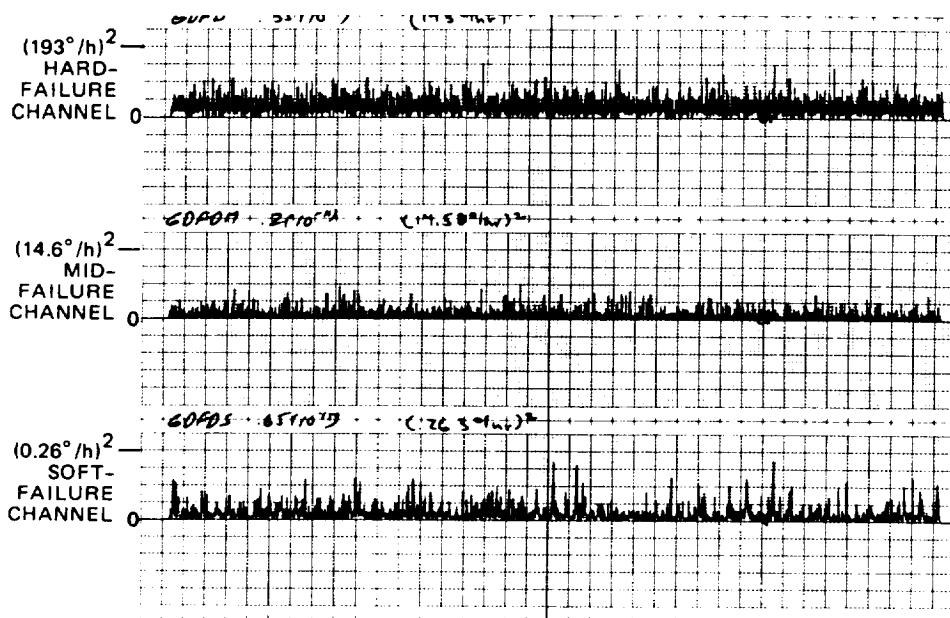
$$T_{g_s} = (0.660°/h)^2$$

$$T_{a_s} = (1967 \ \mu g)^2$$

The actual values of the first failure detected are obtained by modifying these values by the failure-detection sensitivity. These values are 0.835 degree per hour for the gyros and 2488 micro-g for the accelerometers.

9.4   Simulation Results

The failure-decision functions obtained with the GLT algorithm for both the nonmaneuvering and maneuvering trajectories are presented in Figure 18 for the gyros and Figure 19 for the accelerometers. The conclusions that can be drawn regarding these variables and the GLT FDI system are the same as those that were drawn regarding the EVT parity-equation residuals and algorithms presented in Section 8.4. They are not repeated here.

The failure-detection thresholds obtained for the GLT algorithm are presented in Figure 20 for the gyros and in Figure 21 for the accelerometers. The constant portions of the thresholds used to account for high-frequency effects are the same ones used for the EVT algorithm presented in Table 5. The threshold levels obtained for the hard- and mid-failure channels with the GLT algorithm are the same as those obtained with the EVT algorithm. The soft-failure detection levels are slightly

Figure 18.   TDOF gyro failure-decision functions:
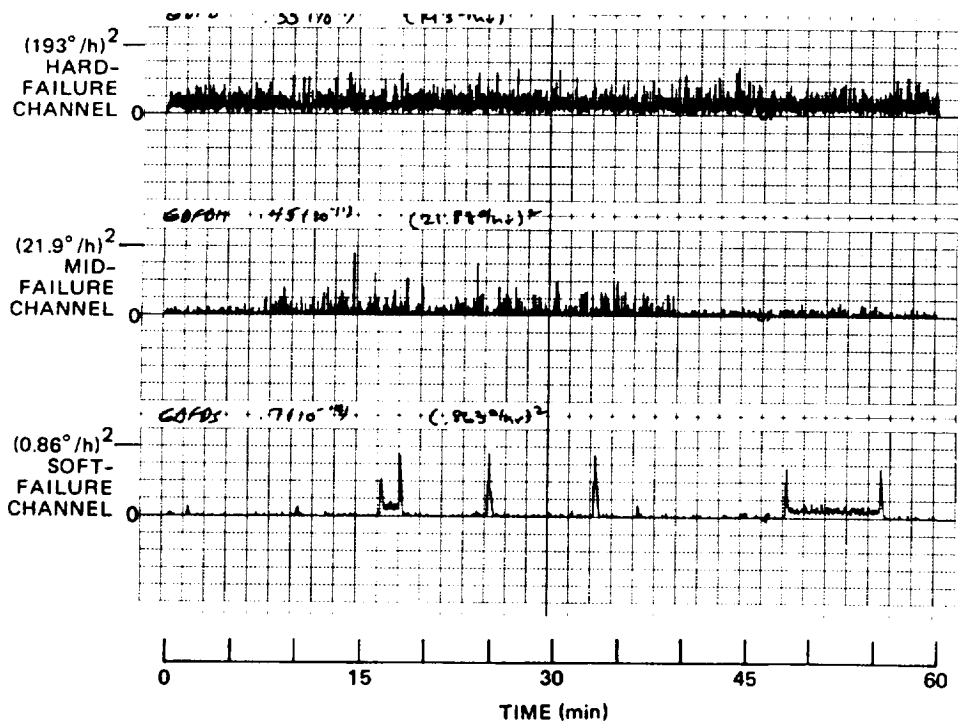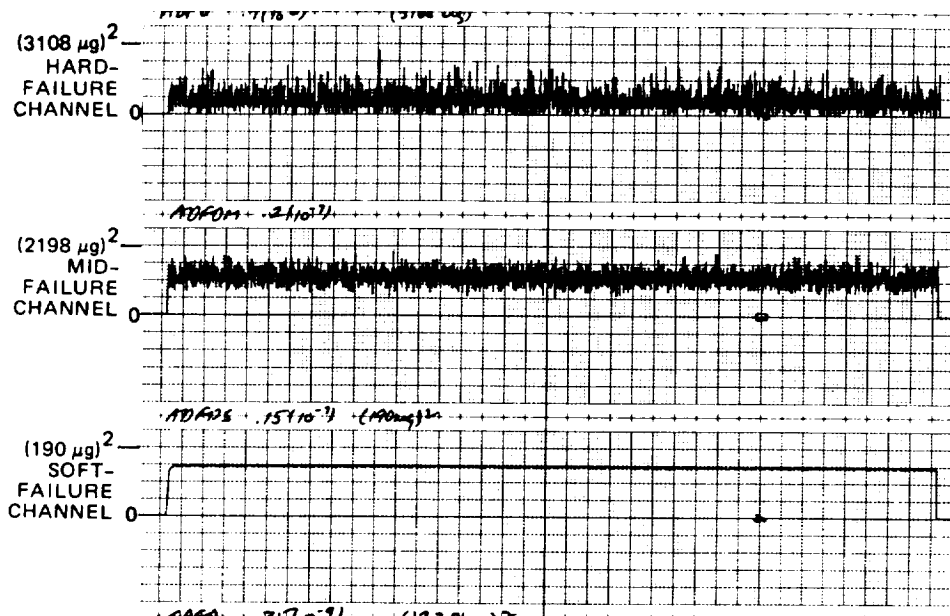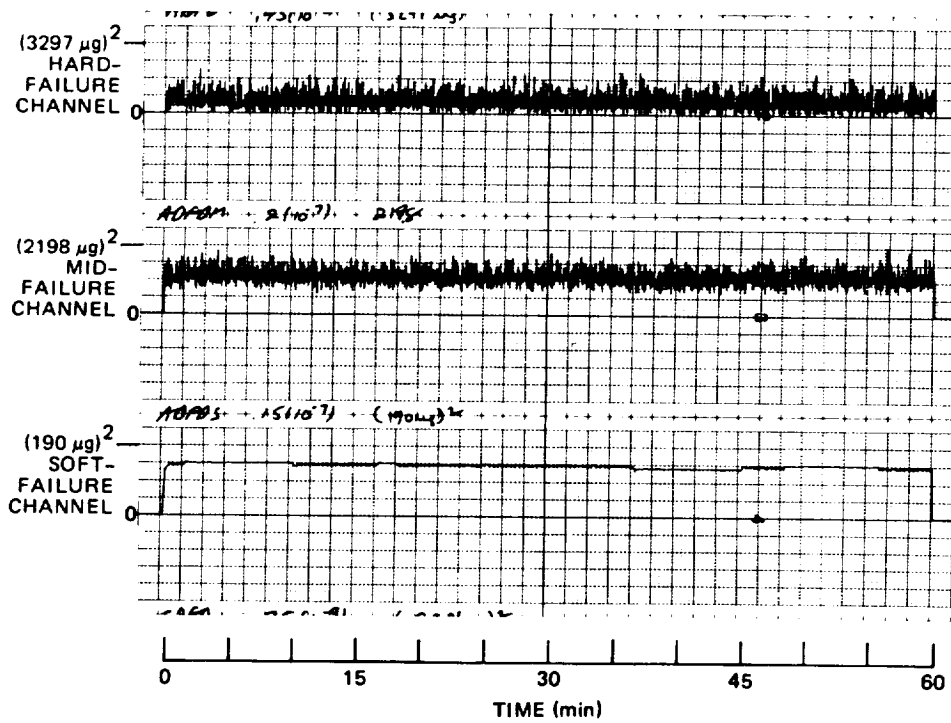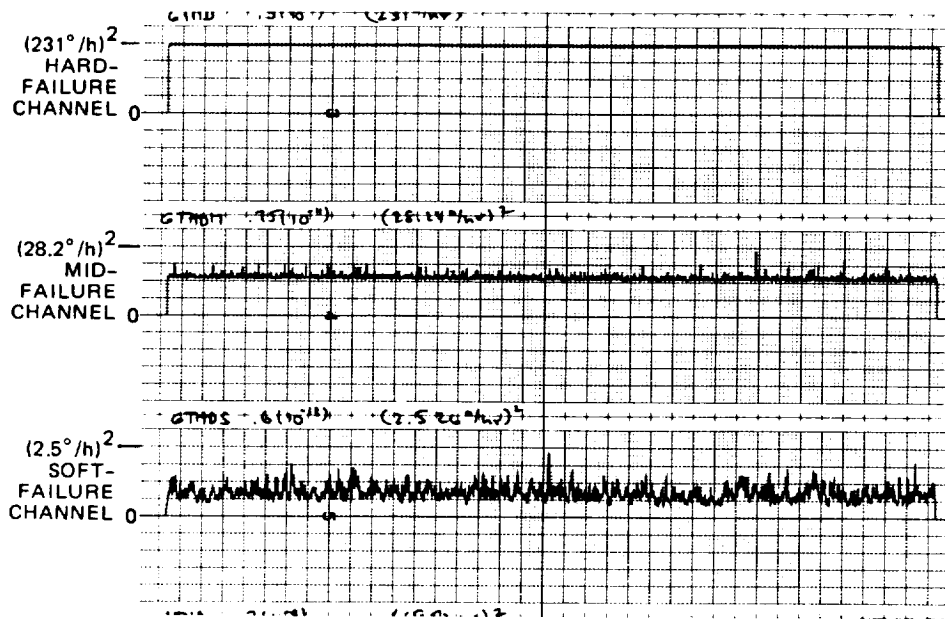GLT, no sensor failure.

Figure 19. Accelerometer failure-decision functions:
GLT, no sensor failure.

71

STRAIGHT, LEVEL FLIGHT

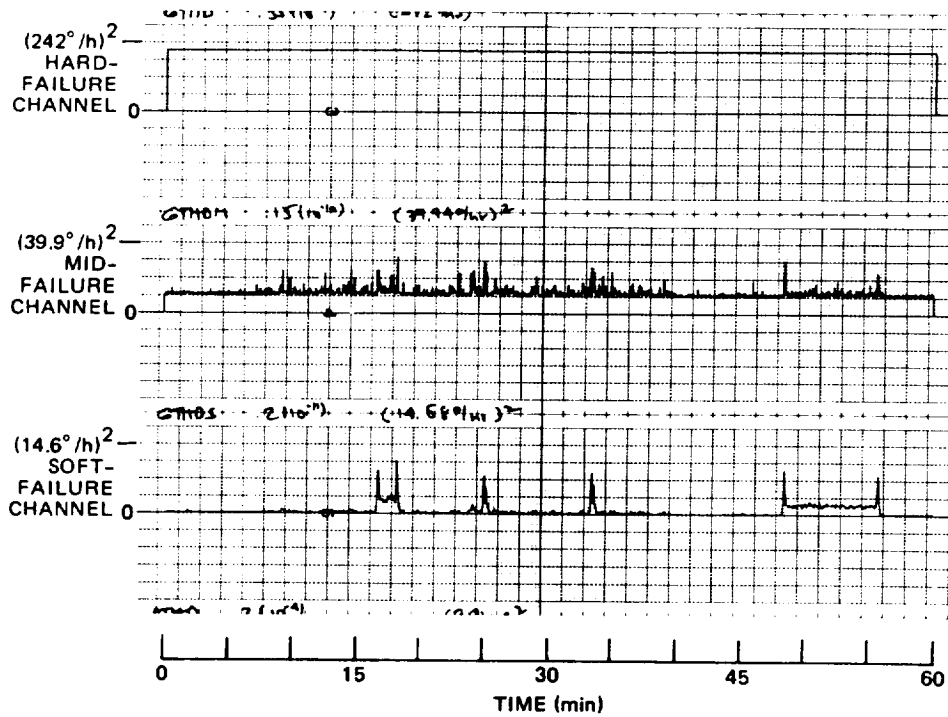

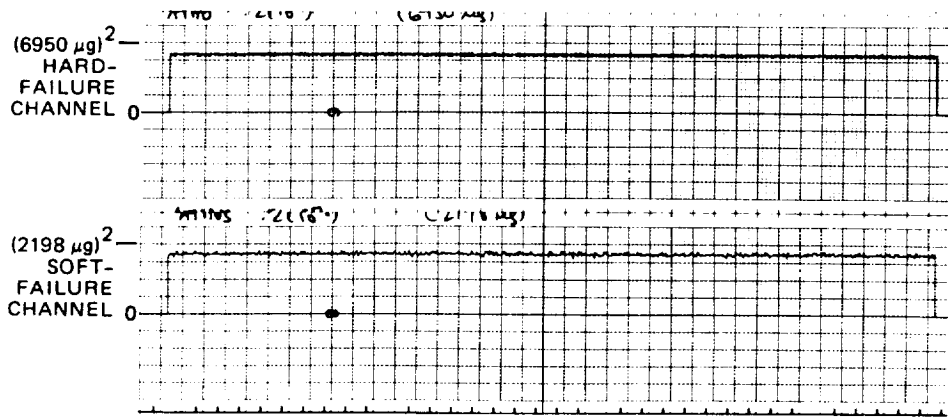**DYNAMIC TRAJECTORY**

TIME (min)

Figure 20.   TDOF gyro failure-detection thresholds: GLT.

STRAIGHT, LEVEL FLIGHT

DYNAMIC TRAJECTORY

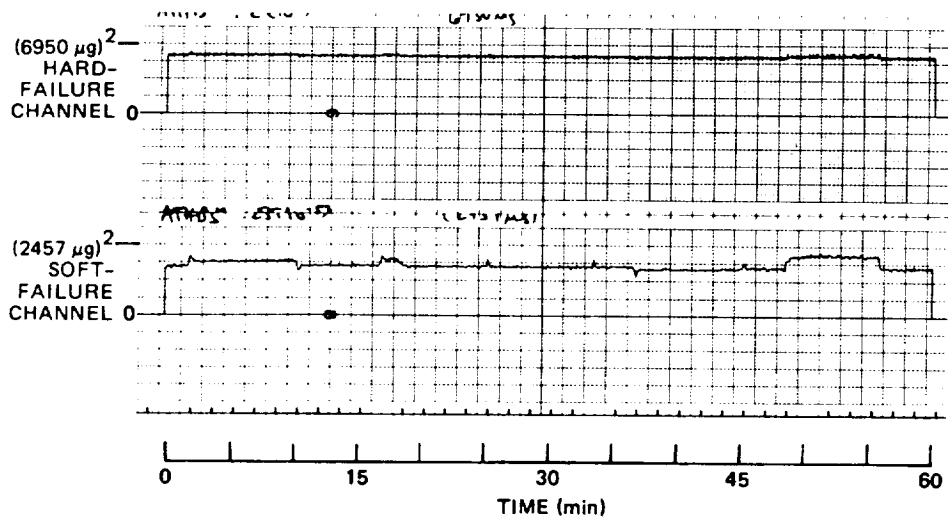

Figure 21. Accelerometer failure-detection thresholds: GLT.

73

greater for the GLT algorithm, with the base level being ≈1.0 degree
per hour for the gyros and ≈1966 micro-g for the accelerometers. This
conclusion reinforces a similar conclusion concerning the relative values
of the ideal failure-detection levels of the GLT and EVT algorithms.
The 1-degree-per-hour soft-failure-detection level is greater than the
ideal level of 0.66 degree per hour. Without turbulence, this level was
lowered to 0.71 degree per hour.

SECTION 10

A COMPARISON OF THE EVT AND GLT ALGORITHMS

A comparison may be drawn between the EVT and GLT algorithms based upon the results presented in this report. There are advantages and disadvantages to both approaches.

Consider first the failure-detection capability of the two algorithms: uniform detectability of the first failure exists with both algorithms. The level of failure detected was the same for both systems for the hard- and mid-failure channels. At first glance, the results of Sections 8.3 and 9.3 imply that the edge-vector approach results in a slightly better soft-failure-detection capability for the first sensor failure. For example, the level of first failure which can be detected is 0.64 degree per hour for the EVT and 0.835 degree per hour for the GLT. This comparison is not quite fair, however, in that the performance of the FDI system is not considered. The probability of correct detection, missed alarm, etc., has not been taken into account. Therefore, a comparison based on the thresholds obtained directly via the technique presented can be misleading.

In addition, for a given threshold, smaller failures are detected with the GLT algorithm. Furthermore, the thresholds for the GLT algorithm decrease as a function of the number of good instruments remaining in the cluster and the number of parity equations. This is not true for the thresholds associated with the EVT algorithm. The failure-detection sensitivity for both the GLT and EVT algorithms lessens with fewer instruments remaining in the cluster. For the thresholds determined in

75

this study, it can easily be shown that it is then possible to detect smaller failures with the GLT algorithm than with the EVT algorithm when fewer sensors are present in the cluster. Consider the case of detecting the third failure. For the GLT algorithm, the ideal threshold will be reduced by $\sqrt{1/5}$ (see Eq. (13)) to a value of 0.295 degree per hour, since only one parity equation is used. The ideal threshold for the EVT algorithm remains the same. The minimum failure-detection sensitivity is 0.1830 for the GLT algorithm and 0.2558819 for the EVT algorithm. There-fore, the largest third failure not detected by the GLT algorithm is 1.612 degrees per hour, while failures up to 1.749 degrees per hour may go undetected with the EVT algorithm.

Additional qualitative comparisons of the FDI capability possible with the EVT and GLT algorithms can be made from a consideration of Sections 8.2 and 9.2. The FDI capability associated with the GLT algo-rithm has the advantage of being more uniform, particularly for the first and second failures. This is based on the failure-detection sensitivity coefficients presented in Tables 4 and 8. It is only when the third failure is being detected that a small failure-detection sensitivity occurs for the GLT algorithm. In contrast, a small failure-detection sensitivity occurs when detection of the second failure with the EVT algorithm is attempted.

It also appears that the GLT is superior to the EVT with regard to the wrong isolation of single-axis failures. This conclusion comes from a consideration of Tables 4 and 9 and the discussion associated with them. The probability of the wrong isolation of a failure should be less for the GLT algorithm than for the EVT algorithm because of the large differ-ence in the magnitude of the isolation coefficients given in Table 9. For the EVT, the probability of wrong failure isolation appears to be much greater as indicated by the discussion in Section 8.2. It is only with the isolation of the second failure that the GLT appears vulnerable to wrong isolation, but the EVT also suffers in this regard. It is felt that the GLT algorithm is superior to the EVT algorithm in its ability to correctly isolate the second failure.

The EVT algorithm appears to have an advantage in terms of computer memory required. The GLT algorithm requires that different sets of parity equations be stored. In addition, the switching logic that goes along with the selection of the proper set of equations and the ordering of the sensors associated with the use of these equations could be quite complex. The EVT is very straightforward from this point of view. However, computer memory is rarely a limiting factor with regard to system software. The major limitation arises because of the throughput required with repetitive calculations. It is on this basis that the software requirements of the two algorithms will be judged. The two algorithms appear to be about equal in this respect.

The two algorithms also have the ability to detect TDOF failures. The EVT is transparent to most TDOF failures as both axes are included in any parity equation using a given sensor. For the GLT, the failure-decision function is the same for SDOF and TDOF failures. However, different failure-isolation decision functions exist as given by Eq. (12) and (13).

In the case of a null failure, where a sensor yields a zero output, both algorithms should function properly and detect and isolate the correct failure. This has been demonstrated via simulation. The reason that this is true is that the basic property of a parity-equation system, i.e., $\hat{V}\hat{H} = 0$, no longer holds. The introduction of a null failure may be looked upon as the introduction of a failure of the opposite sign and magnitude equal to the parity-equation element times the failed-sensor output. For example, the first parity equation for the GLT algorithm may be written as

$$\rho_1 = V_{11}m_1 + V_{12}m_2 + \ldots + V_{1n}m_n$$

If m_1 fails (goes to zero) the $V_{11}m_1$ term disappears. This may also be interpreted as the introduction into the system of a failure of magnitude $-V_{11}m_1$. A failure of this magnitude is large enough that detection and isolation should be relatively easy.

77

SECTION 11

SUMMARY AND CONCLUSIONS

The major result of this study was the demonstration of the feasibility of performing FDI for the redundant IMU of interest in an air-transport-vehicle environment. Acceptable performance was obtained for a range of failures from hard (or extremely large ones) down through the soft ones which affect the navigation performance of the system. The detection and isolation of failures down to the range of 0.5 degree per hour for the gyros and 1500 micro-g for the accelerometers was clearly demonstrated.

In addition, a methodology was developed for the design and evaluation of fault-tolerant systems for the redundant IMU. This methodology can be used as a baseline for the development of a more refined algorithm which considers the specific characteristics of the instruments to be used in the actual system and the physical separation of the components of the IMU as they will actually be implemented in the vehicle.

The development of failure-detection thresholds was a major consideration in the development of the FDI system. The need for dynamic failure-detection thresholds was demonstrated, particularly for the soft-failure gyro FDI channel. An algorithm was developed for the generation of these thresholds as a function of the vehicle environment. The thresholds consist of a constant portion to account for high-frequency sensor noise and a dynamic portion to account for the effects of vehicle dynamics.

The FDI system for the gyros could possibly require only constant thresholds for the hard- and mid-failure channels. The capability for the channels was shown to be ≅250 degrees per hour for the hard failures and ≅36 degrees per hour for the mid-value failures. Dynamic thresholds are needed for the soft-failure channel, with detectability in the range of 0.5 to 0.7 degree per hour possible. It was not possible to give an advantage to either algorithm since the probabilities of FDI system performance were not accounted for.

The accelerometer FDI system has its own unique characteristics. Constant thresholds could quite possibly be used for the whole system. Since the hard-failure-detection level is low (≅8000 micro-g), the need for a mid-failure channel is moot. A soft-failure-detection capability in the vicinity of 1500 micro-g was demonstrated.

The GLT and EVT algorithms were compared from the standpoint of their FDI capability. Approximately the same failure-detection capability was achieved with both algorithms. However, the GLT has an advantage with regard to the detection of the second and third soft failures, since the thresholds for this algorithm decrease as a function of the number of sensors remaining in the system. This helps to offset the decrease in failure-detection sensitivity which comes about with fewer sensors. It was also shown that the failure-detection sensitivity of the GLT algorithm is more uniform than that of the EVT. The GLT algorithm also has an advantage over the EVT algorithm with regard to the ability of the algorithm to correctly isolate a sensor failure. Finally, it should be noted that both the algorithms will be unaffected by most credible TDOF sensor failure modes. The same is true for null failures.

The EVT algorithm will require less computer memory than the GLT algorithm. This is not a major advantage, however, since computer throughput is the limiting factor in software design and implementation.

LIST OF REFERENCES

1. Preliminary Design of a Redundant Strapped Down Inertial
    Navigation Unit Using Two-Degree-of-Freedom Tuned-Gimbal
    Gyroscopes, NASA CR-145305, October 1976.

2. Daly, K., et al., Development of Capability for Multifunction
    Integrated Reference Assembly Evaluation, AFAL-TR-77-64,
    July 1977.

3. Motyka, P., et al., Multifunction Inertial Reference Assembly
    Technology (MIRAT) Simulation Development, Configuration
    Evaluation and Test Plan Development, AFAL-TR-78-33, March 1978.

4. Burns, R., Multifunction Inertial Reference Assembly (MIRA)
    Vol. I Multi-function Inertial Reference Assembly Final Report,
    AFFDL-TR-78-105, September 1978.

5. Baum, R., E. Morrison, and R. Peters, "A Redundant Inertial
    Navigation System for IUS", AGARD Conference Proceedings, No. 272,
    August 1979.

6. Daly, K., E. Gai, and J. Harrison, "Generalized Likelihood Test
    for FDI in Redundant Sensor Configurations", AIAA Journal of
    Guidance and Control, Vol. 2, No. 1, January-February 1979,
    pp. 9-17.

7. Gai, E., J. Harrison, and K. Daly, "FDI Performance of Two
    Redundant Sensor Configurations", IEEE Transactions of Aerospace
    and Electronic Systems, Vol. AES-15, No. 3, May 1979.

LIST OF REFERENCES (Cont.)

8.   Motyka, P., and J. Bell, Failure Detection and Isolation for
     Tactical Aircraft Using the Generalized Likelihood Test, NAECON,
     May 1980 (also CSDL Report P-983).

9.   "Inertial Upper Stage (IUS) Full Scale Development Phase",
     Redundant Inertial Measurement Unit (RIMU) Failure Detection and
     Analysis Report, Hamilton Standard Electronics System Report
     No. HSER 6930, October 1978.

10. Daly, K., J. Harrison, and E. Gai, "The Effect of Filtering
     upon Parity Vector Noise Standard Deviation", CSDL Memorandum,
     June 1979.

11. Potter, J., and M. Suman, "Thresholdless Redundancy Management
     with Arrays of Skewed Instruments", Integrity in Electronic
     Flight Control Systems, Agardograph-224, 1977.

12. Redundant IMU Instrument Orientation Requirements for IUS, CSDL
     Report R-1076, March 1977.

1. Report No. NASA CR-165658	2. Government Accession No.	3. Recipient's Catalog No.
4. Title and Subtitle FAILURE DETECTION AND ISOLATION ANALYSIS OF A REDUNDANT STRAPDOWN INERTIAL MEASUREMENT UNIT		5. Report Date February 1981
		6. Performing Organization Code
7. Author(s) P. Motyka, M. Landey, R. McKern		8. Performing Organization Report No. R-1414
9. Performing Organization Name and Address The Charles Stark Draper Laboratory, Inc. 555 Technology Square Cambridge, Massachusetts 02139		10. Work Unit No.
		11. Contract or Grant No. NAS1-15933
12. Sponsoring Agency Name and Address National Aeronautics and Space Administration Washington, D.C. 20546		13. Type of Report and Period Covered Final Report October 1979-December 1980
		14. Sponsoring Agency Code

15. Supplementary Notes

Langley Technical Monitor: Frederick R. Morrell

16. Abstract

The objective of this study was to define and develop techniques which will be the basis for failure-detection and isolation (FDI) algorithms for a NASA-owned dual-fail/operational redundant strapdown inertial navigation system. The FDI techniques chosen include provisions for hard- and soft-failure detection in the context of flight control and navigation. Analyses were done to determine error-detection and switching levels for the inertial nav-igation system, which is intended for a conventional takeoff or landing (CTOL) operating environment. In addition, investigations of false alarms and missed alarms have been included for the FDI techniques developed, along with the analyses of filters to be used in conjunction with FDI processing. Two specific FDI algorithms were compared in this study: the Generalized Like-lihood Test and the Edge Vector Test. A deterministic digital computer simulation was used to compare and evaluate the algorithms and FDI systems.

17. Key Words Suggested by Author Failure Detection and Isolation Redundant Inertial Measurement Unit		18. Distribution Statement Unclassified - Unlimited		
19. Security Classif. (of this report) Unclassified		20. Security Classif. (of this page) Unclassified	21. No. of Pages	22. Price